

Electronic Thesis and Dissertation Repository

8-9-2021 10:00 AM

Frequency dependent diffusion kurtosis measurement in the human brain with oscillating gradients

Kevin B. Borsos, *The University of Western Ontario*

Supervisor: Baron, Corey A., *The University of Western Ontario*

A thesis submitted in partial fulfillment of the requirements for the Master of Science degree in Medical Biophysics

© Kevin B. Borsos 2021

Follow this and additional works at: <https://ir.lib.uwo.ca/etd>



Part of the [Bioimaging and Biomedical Optics Commons](#), and the [Medical Biophysics Commons](#)

Recommended Citation

Borsos, Kevin B., "Frequency dependent diffusion kurtosis measurement in the human brain with oscillating gradients" (2021). *Electronic Thesis and Dissertation Repository*. 8012.
<https://ir.lib.uwo.ca/etd/8012>

This Dissertation/Thesis is brought to you for free and open access by Scholarship@Western. It has been accepted for inclusion in Electronic Thesis and Dissertation Repository by an authorized administrator of Scholarship@Western. For more information, please contact wlsadmin@uwo.ca.

Abstract

Oscillating gradient spin-echo (OGSE) is an implementation of diffusion MRI that enables shorter effective diffusion times than the conventional pulse gradient spin-echo (PGSE) by periodically modulating the diffusion gradient. Measurements of the diffusion kurtosis, which reflects the degree of restricted diffusion, have previously been prohibited with OGSE due to technical limitations of clinical gradient systems. This thesis presents a novel oscillating gradient waveform that enables the measurement of kurtosis using OGSE without requiring advanced gradient hardware. Decreases of kurtosis are observed in OGSE acquisitions of healthy subjects relative to PGSE, demonstrating the dependence of the kurtosis on oscillation frequency. This frequency dependence is exploited to generate novel contrast based on the difference between PGSE and OGSE kurtosis measurements acquired with an optimized protocol. This work demonstrates the first in vivo measurements of kurtosis in the human brain using OGSE without the aid of advanced gradient hardware.

Keywords: Diffusion MRI, Oscillating Gradient Spin-Echo, Kurtosis, Ultra-high field MRI, Optimization.

Summary for lay audience

Magnetic resonance imaging (MRI) is a diagnostic imaging modality that can image soft tissues for the characterization of anatomy and diagnosis of disease. Diffusion MRI is a particular type of MRI that can image water molecules in the body that are randomly moving due to thermal energy. When molecules diffuse they often bounce off boundaries like cell membranes and other structures they encounter as they move, therefore by following the diffusion of water molecules it is possible to gain insight into cellular structures that make up the surrounding environment. Oscillating gradient spin-echo (OGSE) is a specialized diffusion MRI method that can control the time the tracked molecules are allowed to diffuse for. By looking at diffusion using different diffusion times more insight about cellular structures can be acquired; a short diffusion time gives less time for the molecule to explore surrounding structures while a long diffusion time means the molecules will interact with many structures.

This thesis presents a method to apply OGSE in the human brain to measure a quantity called the diffusion kurtosis, which provides information about how restricted diffusion is. Previously, measuring the kurtosis with OGSE was not possible due to technical limitations however in this work a new implementation of OGSE is proposed that allows the kurtosis to be measured on clinical MRI scanners. By using OGSE a new type of contrast can also be generated by calculating the difference in kurtosis values between the images taken with two different diffusion times. This type of contrast has been observed in animals before but never in humans and is a candidate for being sensitive to stroke and brain tissue degeneration. The new method presented here will allow us to begin exploring new diagnostic applications of the diffusion kurtosis with OGSE in humans in future studies.

Co-Authorship Statement

The work presented in Chapter 2 of this thesis is adapted from a manuscript to be submitted entitled "Bipolar oscillating gradients for mapping diffusion kurtosis dispersion in the human brain" authored by Kevin B. Borsos, Desmond H.Y. Tse, Paul I. Dubovan and Corey A. Baron. As the primary author, I contributed to all aspects of this study including the conception of the gradient waveform, experimental study design, data acquisition and analysis and writing of the manuscript. Complete author contributions are as follows: K.B.Borsos - Conceptualization, Data curation, Formal analysis, Investigation, Methodology, Software, Study Design, Writing - original draft and Writing - review & editing. D.H.Y. Tse - Software and Methodology. P.I. Dubovan - Data curation. C.A. Baron - Conceptualization, Funding acquisition, Investigation, Resources, Study Design, Supervision, Writing - review & editing.

Acknowledgments

I would like to begin by thanking my supervisor, Dr. Corey Baron. Corey, I'd like to thank you from the bottom of my heart for taking the time to train me in a field that I truly had no experience in, for always being available (even when you weren't) and for believing in our project (even if at times I didn't). I will always be grateful for your support, for always answering my often trivial questions and for giving me the freedom to explore my own ideas. I consider myself truly fortunate to have worked under such a supportive and intelligent investigator.

Additionally, I'd also like to thank the members of my advisory committee, Drs. Ali Khan and Robert Bartha for their guidance and support throughout the course of this project. Their comments were always insightful and constructive, sparking discussions that ultimately led to expanding my knowledge and improving my understanding; I'm very grateful for their input.

I also have to thank those who led me to this degree and were a part of the journey. Thanks to the folks at Kumar's lab for teaching me everything I know about making a measurement and for showing me what proper lunchtime banter looks like. I also need to thank the fellas for their support, for always keeping me laughing and for providing some much needed perspective at times. Additionally, I wish to thank my lab mates, Farah, Gab, Jake, Naila, Nico, Paul and Tales for their help and assistance over the past couple of years. Whether that was answering questions, providing feedback or bouncing off ideas, I'm very grateful to have worked alongside such a well versed group of young scholars.

In addition, this work could not have been completed without the timely and indispensable assistance of the staff at CFMM and Robarts. Thanks to Scott Charlton and Trevor Szekeres for assisting with scans and for their patience during debugging. I'd also like to thank Sue Bedford for facilitating our bookings and providing assistance whenever I needed it.

I'd like to also thank my thesis examiners Drs. Charles McKenzie, Alexei Ouriadov and Jonathan Thiessen for their thorough and constructive evaluation of this thesis and for providing excellent feedback to improve it. Similarly, I'd also like to thank my exam chair Dr. Ravi Menon for taking the time to facilitate my examination and ensuring organized and timely discussions.

Finally I'd like to thank my family for their support and encouragement during these past couple of years. In particular my parents who truly gave everything they could to help me succeed; words cannot express all that you gave to both your children, köszönöm.

Table of Contents

Abstract	i
Summary for lay audience	ii
Co-Authorship Statement	iii
Acknowledgments	iv
List of Figures	viii
List of Abbreviations	xi
Preface	xii
1 Introduction	1
1.1 Diffusion	1
1.2 Biological Diffusion	3
1.3 Diffusion MRI	6
1.3.1 Sensitizing MRI to Diffusion	6
1.3.2 Diffusion Attenuated Signal	10
1.3.3 Apparent Diffusion Coefficient	11
1.3.4 Diffusion Kurtosis	15
1.4 Oscillating Gradient Diffusion MRI	19
1.4.1 Oscillating Gradient Spin-Echo (OGSE)	21
1.4.2 Applications and Current Progress	24
1.4.3 Limitations	27
1.4.4 Summary	30
2 Bipolar oscillating gradients for mapping diffusion kurtosis dispersion in the human brain	32
2.1 Introduction	32
2.2 Methods	35
2.2.1 Gradient Waveform Design	35
2.2.2 Monte Carlo Optimization	37
2.2.3 In Vivo Protocol	39
2.2.4 Image Analysis	40
2.2.5 Re-test Analysis	41

2.3	Results	41
2.3.1	Optimization Results	41
2.3.2	in vivo Results	42
2.4	Discussion	48
2.4.1	Waveform Remarks	48
2.4.2	In Vivo Findings	49
2.4.3	Applications	50
2.5	Conclusion	51
3	Conclusions	53
3.1	Overview and Objective	53
3.2	Findings and Limitations	54
3.3	Future Work	55
A		56
A.1	Derivation of Equation 2.2	56
	Bibliography	58

List of Figures

1.1	Gaussian probability distribution indicating likelihood of a molecule diffusing a given distance in a fixed observation time t ; the MSD is described by the variance of the distribution. Shown curves were generated using a diffusion coefficient of $3 \times 10^{-3} \text{ mm}^2/\text{s}$	2
1.2	(A) Visual representation of "random walk" diffusion trajectories for both restricted (red) and hindered (blue) diffusion regimes. The black boundaries, representative of cell membranes act to restrict the movement of diffusing molecules. (B) Resultant time trends in mean-squared displacement for free, hindered and restricted diffusion regimes. Note for restricted diffusion a terminal MSD is reached based on the restricting boundary.	4
1.3	Labeled diagram of a human neuron demonstrating the long and narrow geometry of axons and more dispersed nature of dendrites. Image © Arizona Board of Regents / ASU Ask A Biologist, licensed under CC-BY-SA 3.0. Accessed via www.askbiologist.asu.edu/neuron-anatomy	5
1.4	Spin dephasing behaviour for a typical diffusion sequence. Static spins experience dephasing due to gradients alone which is reverted by the second gradient. Diffusing spins experience additional dephasing due to thermal displacements which is not reverted by the second diffusion gradient resulting in signal loss. As shown δ corresponds to the gradient duration, Δ denotes the gradient duration plus the time which separates the two diffusion gradients and G denotes the gradient amplitude. Figure adapted from Patterson et al. [10]	9
1.5	Diffusion weighted images (DWIs) acquired with PGSE at b-values of 0 (left), 1000 (middle) and 2000 s/mm^2 (right). Images demonstrate decreasing SNR due to increasing signal attenuation with larger b-values (moving from left to right).	11
1.6	Typical diffusion signal curve generated from two b-value acquisitions corresponding to $S(b_1)$ and $S(b_2)$. The ADC is determined as the slope of the linear fit between the natural logarithm of the two points according to equation 1.10.	13
1.7	Comparison of various diffusion metrics and contrasts from a healthy subject. (A) DWI acquired with PGSE at $b = 1000 \text{ s}/\text{mm}^2$, (B) calculated average ADC map and (C) calculated apparent kurtosis map generated from $b = 0, 1000, 2000 \text{ s}/\text{mm}^2$ acquisitions.	14

1.8	Probability distributions that governs the likelihood of a spin diffusing a given distance in a fixed time interval, for both zero kurtosis (pink) and positive kurtosis (blue). The narrowing of the probability distribution for positive kurtosis signifies restricted diffusion and increased heterogeneity compared to purely Gaussian diffusion which has no kurtosis. Image courtesy of Allen D. Elster, MRIquestions.com	17
1.9	Natural logarithm of the diffusion signal across a wide range of b-values. The linear approximation of equation 1.8 is valid up to $b \sim 1000 \text{ s/mm}^2$. Higher order effects are observed for $b > 1000 \text{ s/mm}^2$ where the signal begins to deviate from the first-order linear approximation due to kurtosis effects and is better described by the additional term in equation 1.12.	18
1.10	Visual representation of possible random walk trajectories for two relative diffusion times (or conversely two different oscillation frequencies) for both large (top row) and small (bottom row) diameter axons. Red trajectories indicate restricted diffusion, where the diffusion time is long enough to permit the boundary to limit the MSD resulting in reduced ADCs and increased kurtosis. Blue trajectories indicate free unrestricted diffusion resulting in larger ADC values and reduced (or zero) kurtosis. Since the distance to the boundary is less for smaller axons, an even shorter diffusion time would be required to observe differences in the ADC and kurtosis based on changes in the MSD, hence restricted diffusion is implied in small axons for both diffusion times.	20
1.11	Comparison of gradient waveforms for PGSE (A), cosine modulated OGSE (C) and sine modulated OGSE (E). The corresponding normalized gradient modulation spectra are also shown (B,D,F) with cosine modulated demonstrating a non-zero peak frequency corresponding to the oscillation frequency. Waveform polarity is reversed for the second diffusion gradient due to the effects of the refocusing RF pulse (not shown); OGSE waveforms are shown using only 2 periods.	23
1.12	Comparison of PGSE with 40 Hz $N = 2$ and $N = 3$ cosine modulated trapezoidal OGSE. For the same gradient amplitude and slew rate, $N = 2$ OGSE can achieve only $\sim 3\%$ of the b-value possible with a PGSE sequence of equal duration (b_{PGSE}). Increasing the number of oscillation periods (N) can increase the b-value, however addition of extra periods also elongates the gradient duration as shown for $N = 3$	28
2.1	Comparison of new bipolar $N = 1.5$ OGSE waveform (A), $N = 2$ OGSE (B) and PGSE (C) waveforms. Corresponding power spectra (G-I) are also shown demonstrating comparable spectral selectivity between $N = 1.5$ and $N = 2$ OGSE for the target frequency. Also shown is the zeroth moment of each waveform (D-F). Continuous periodicity of the zeroth moment is apparent in the $N = 1.5$ waveform (D) compared to $N = 2$ (E) due to the reduction of the gradient separation time.	36

2.2	SNR of ΔK for varying b-value and frequency combinations (A) and comparisons of maximum possible SNR for $N = 1.5$, $N = 2$ and $N = 2.5$ oscillation periods for both ΔK and ΔADC maps (B).	42
2.3	Generated ADC maps (top row) and apparent kurtosis maps (bottom row) from one healthy subject using both PGSE (A,C) and OGSE (B,D). An increase of ADC in parenchyma is observed in OGSE relative to PGSE in ADC maps and a reduction is demonstrated in apparent kurtosis maps. Also shown in (C) is an example ROI used for calculating mean differences between OGSE and PGSE.	43
2.4	Generated ΔADC (top) and ΔK (bottom) maps for a few slices from each subject. Comparable image quality is observed across participants though some B_0 inhomogeneity induced distortions are apparent.	44
2.5	Sagittal slices of kurtosis dispersion maps showing the corpus callosum of each subject (left) and mean absolute ΔK values of different regions of the corpus callosum averaged across all subjects (right); error bars indicate the standard deviation. There is no statistically significant difference between regions.	45
2.6	Example regions of interest (A) of the internal capsule (green) and posterior white matter (blue) regions. (B) comparison of mean absolute ΔK values across all subjects between the internal capsule (IC) and white matter (WM) ROIs, error bars denote the standard deviation. Here * denotes $p < 0.05$	45
2.7	Comparison of optimal ($b = 2500 \text{ s/mm}^2$, top row) and suboptimal ($b = 2000 \text{ s/mm}^2$, bottom row) ΔK maps from one subject. A qualitative increase in noise is apparent in the suboptimal scans supporting the optimization results.	46
2.8	Bland Altman plots comparing test and re-test acquisitions for the $b = 2000$ (left column) and $b = 2500 \text{ s/mm}^2$ scans (right column) across all volumes from each subject; rows correspond to different subjects, columns correspond to the sub-optimal and optimal protocols. Also shown are the coefficients of variation (CoV) and standard deviations (Std). The dashed lines on each plot denote ± 1.96 standard deviations and the solid black line denotes the mean difference between the test and retest measurements.	47

List of Abbreviations

AD	Axial Diffusivity
ADC	Apparent Diffusion Coefficient
CoV	Coefficient of Variation
CSF	Cerebrospinal Fluid
DKI	Diffusion Kurtosis Imaging
dMRI	Diffusion Magnetic Resonance Imaging
DTI	Diffusion Tensor Imaging
DWI	Diffusion Weighted Image
EPI	Echo Planar Imaging
FA	Fractional Anisotropy
GM	Grey Matter
MD	Mean Diffusivity
MK	Mean Kurtosis
MRI	Magnetic Resonance Imaging
MSD	Mean-Squared Displacement
NMR	Nuclear Magnetic Resonance
OGSE	Oscillating Gradient Spin-Echo
PGSE	Pulsed Gradient Spin-Echo
RD	Radial Diffusivity
RF	Radio Frequency
ROI	Region of Interest
SNR	Signal-to-Noise Ratio
TE	Echo Time
TR	Repetition Time
WM	White Matter

Preface

The brain is arguably the most vital and complex organ in the human body. Despite this however, the structure of the brain and its relation to pathology and development is not fully understood. The complexity, scale and organization of the billions of neurons in our brains compounded by our present inability to individually monitor these structures, is a primary hurdle in our pursuit of understanding the human connectome and diagnosing associated diseases.

While the development of novel neuroimaging modalities including optical and X-ray based technologies continues, no technique has received wider adoption in clinical and research settings than magnetic resonance imaging (MRI). Introduced nearly half a century ago, its impact has revolutionized the study of the brain by providing a tool that enables non-invasive in vivo imaging without the necessity of ionizing radiation, required for alternative techniques such as conventional radiography or computed tomography. MRI has since been refined to become a robust and reliable tool to image soft tissue across the whole body however this work will focus on it's application to the human brain.

While the physical principals behind magnetic resonance and MRI are rich and insightful, to maintain readability and avoid excessive length, these principals are not extensively presented in this thesis. Rather, the author would refer readers to the following references that were particularly helpful for this work in providing exceptionally informative and in-depth discussions of the physics of MRI and fundamentals of image acquisition:

- Brown, Robert W., Y-C. Norman Cheng, E. Mark Haacke, Michael R. Thompson, and Ramesh Venkatesan. *Magnetic resonance imaging: physical principles and sequence design*. John Wiley & Sons, 2014.
- Bernstein, Matt A., Kevin F. King, and Xiaohong Joe Zhou. *Handbook of MRI pulse sequences*. Elsevier, 2004.

Chapter 1

Introduction

1.1 Diffusion

Diffusion describes the random movement of molecules due to thermal motion. The intrinsic energy possessed by a molecule or particle at any temperature above absolute zero results in randomized motion and is responsible for numerous biochemical and physical processes. This effect was initially observed by Robert Brown in 1827 [1], who noted the agitation of pollen molecules submerged in water when viewed below a microscope; consequently this random movement phenomenon is often referred to as Brownian motion.

The evolution of a given concentration of particles due to Brownian motion can be described by Fick's second law (also known as the diffusion equation):

$$\frac{\partial\varphi(x,t)}{\partial t} = D\frac{\partial^2\varphi(x,t)}{\partial x^2} \quad (1.1)$$

where D is the diffusivity (also called the diffusion coefficient) and φ is the local concentration of molecules. However, Einstein demonstrated that in the absence of a concentration gradient (i.e. self-diffusion) equation 1.1 still applies [2]. In this case however, the stochastic nature of diffusion becomes apparent and $\varphi(x,t)$ is interpreted as the probability of finding a molecule at location x and time t . For the case of a free particle

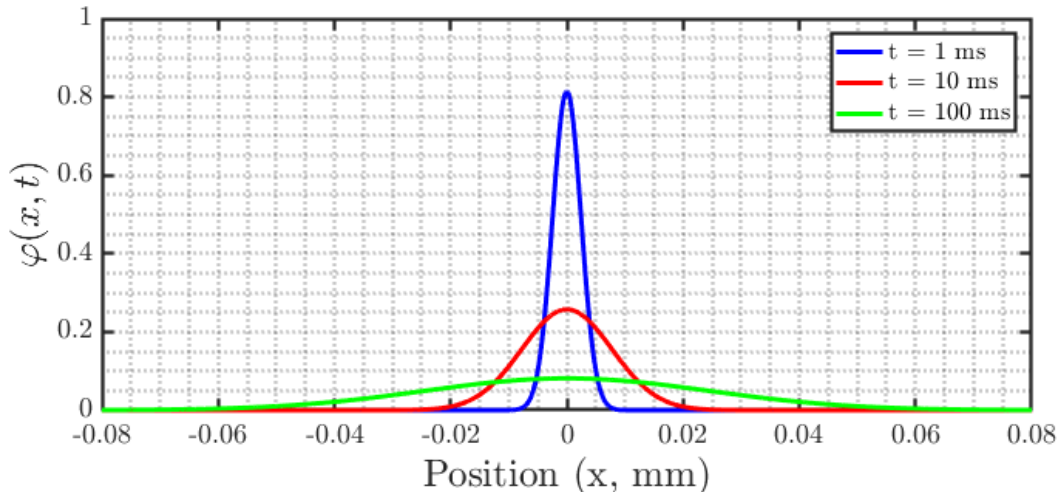


Figure 1.1: Gaussian probability distribution indicating likelihood of a molecule diffusing a given distance in a fixed observation time t ; the MSD is described by the variance of the distribution. Shown curves were generated using a diffusion coefficient of $3 \times 10^{-3} \text{ mm}^2/\text{s}$

whose displacement is not limited by an external barrier, boundary or force the particle's displacement is governed by a Gaussian probability distribution obtained from solving Fick's second law (1.1):

$$\varphi(x, t) = \frac{1}{\sqrt{4\pi Dt}} e^{-\frac{x^2}{4Dt}} \quad (1.2)$$

Particles that obey this relation are said to be undergoing free diffusion (sometimes called Gaussian diffusion based on the functional form). Equation 1.2 may also be referred to as the diffusion propagator and features prominently in theoretical discussions of diffusion. This multivariate expression depends on both space (x) and time (t) with its evolution in both dimensions shown in Figure 1.1. The variance of this distribution:

$$\langle x^2 \rangle = 2Dt \quad (1.3)$$

represents the mean-squared displacement (MSD) of the molecule over a fixed time interval of duration t where D is the diffusion coefficient.

The diffusion coefficient D will have units of $\text{length}^2/\text{time}$ and hence intuitively describes the MSD per unit time. Its value is determined based on the temperature of the

molecule T , the resistance it experiences as it moves through the medium ζ (based on the Stokes drag) and the Boltzmann constant k_B according to the equation:

$$D = \frac{\zeta}{k_B T} \quad (1.4)$$

While the Equipartition theorem describes the relationship between energy and temperature, it was Einstein who first related temperature to displacement through equations 1.3 and 1.4. Notably equation 1.3 also relates the duration of the diffusion process to the MSD of the molecule through the diffusion coefficient. This effect is evident in Figure 1.1 where the MSD, represented as the full width at half maximum, increases with increasing diffusion time. This is a key premise and will be touched upon throughout this work, in particular in sections 1.2 and 1.4 regarding time-dependent diffusion.

1.2 Biological Diffusion

Despite being well characterized, not all diffusion processes can be classified as purely Gaussian. In biological systems free diffusion is in fact scarcely found; the presence of membranes, organelles and molecules often interfere with diffusive movement. These obstacles give rise to two non-Gaussian diffusion regimes termed *hindered* and *restricted* diffusion. When a molecule's movement is rigidly confined, for example when bound within an impermeable membrane, irrespective of the time allowed to diffuse it can never travel beyond this boundary and hence it is said to be undergoing restricted diffusion. However if that same membrane now featured several small pores the molecule would (in theory) be able to escape the boundary should it happen to diffuse through a pore. However, since there are only few pores it is more probable that the molecule remains within the boundary. In this second example, the molecule's movement is not strictly prohibited but rather impeded and hence this is known as hindered diffusion. Experimentally these regimes can be distinguished at long time scales where the restrictive nature

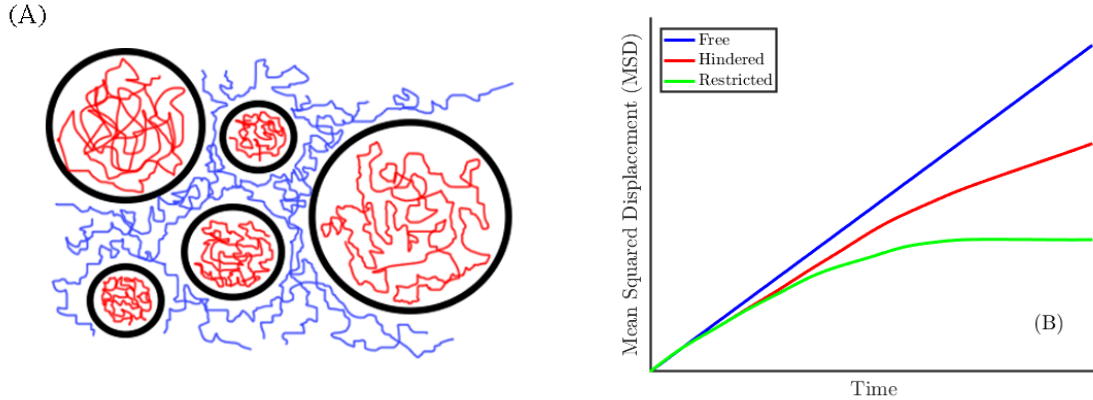


Figure 1.2: (A) Visual representation of "random walk" diffusion trajectories for both restricted (red) and hindered (blue) diffusion regimes. The black boundaries, representative of cell membranes act to restrict the movement of diffusing molecules. (B) Resultant time trends in mean-squared displacement for free, hindered and restricted diffusion regimes. Note for restricted diffusion a terminal MSD is reached based on the restricting boundary.

of boundaries can manifest their effects on limiting the maximum MSD. The visual distinction between hindered and restricted diffusion in a cellular context is presented in Figure 1.2A while Figure 1.2B demonstrates the dependence of the MSD on the diffusion time for each of the three regimes discussed thus far.

Contrary to the simplistic representations of Figure 1.2A, not all cells can be modeled as spherical or symmetric. In particular the neurons that constitute the electrically excitable nerve cells in the brain are highly asymmetric as seen in the diagram of Figure 1.3. While dendrites fan out, axons are long cylindrical-like structures surrounded by a myelin sheath to enhance conductivity. Bundles of myelinated axons are tightly grouped together to form tracts that largely constitute white matter (WM) while dendrites and cell bodies of axons make up the majority of grey matter (GM) [3]. While the characterization of the brain on a cellular or neurological level is beyond the scope of this work, the key attribute of these cells from a diffusion standpoint is their geometry.

The long cylindrical-like shape of axons implies that diffusion is not symmetric along the radial and axial directions. In this configuration because the radius is much smaller than the length, a molecule diffusing within an axon will travel further axially than

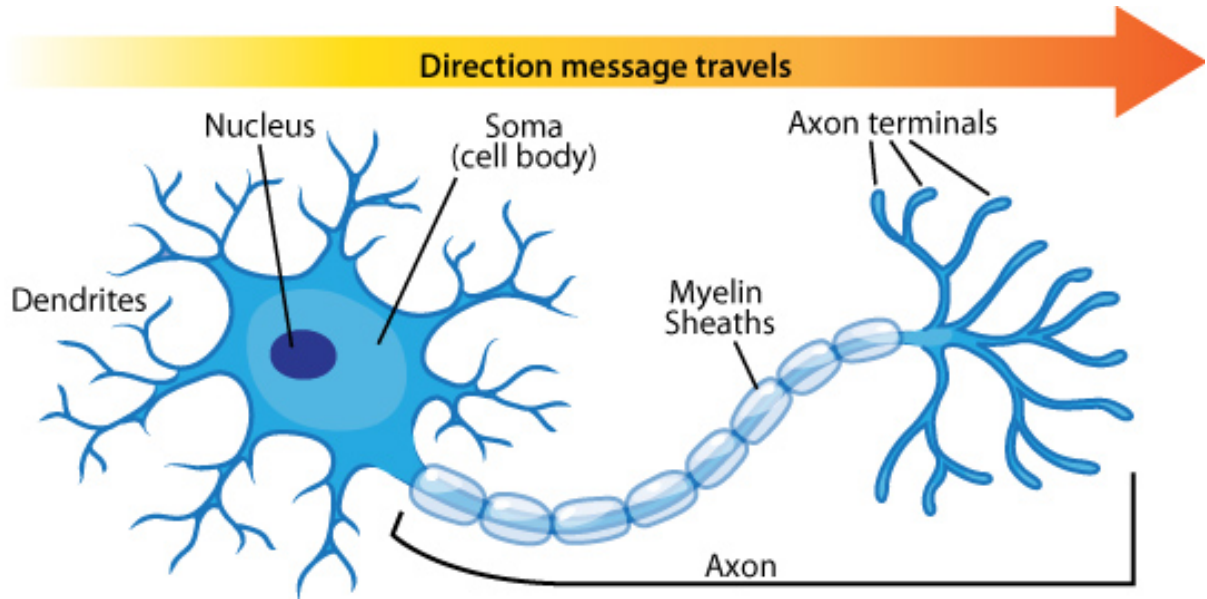


Figure 1.3: Labeled diagram of a human neuron demonstrating the long and narrow geometry of axons and more dispersed nature of dendrites. Image © Arizona Board of Regents / ASU Ask A Biologist, licensed under CC-BY-SA 3.0. Accessed via www.askabiologist.asu.edu/neuron-anatomy

radially in the same time interval. This disparity leads to a directionally dependent diffusion known as anisotropic diffusion (not to be confused with the image processing technique of the same name). Anisotropic diffusion occurs when the Brownian motion of a molecule cannot be described by a single diffusion coefficient but rather requires multiple diffusion coefficients (one for each direction of diffusion) [4]. In the example of an axon, the radial diffusivity can be nearly four times smaller than the axial diffusivity due to the constraints imposed by the cylinder-like geometry [5]. While anisotropy implies directional dependence, isotropic diffusion is synonymous with free diffusion and hence a single diffusion coefficient is adequate to describe diffusion in every direction. The concepts of isotropic and anisotropic diffusion will be featured throughout this work and are key to the large-scale physiological interpretation of diffusion MRI data.

For a more in-depth understanding and detailed review of cellular diffusion and its biophysical role in vivo, the author found references [4,6,7] to be particularly helpful.

1.3 Diffusion MRI

A large percentage of the human body is composed of water and as such, fluids are constantly in flux in our organs and cells. Whereas conventional MRI can image the spatial location of water molecules by monitoring the hydrogen (often referred to as just proton) signal, diffusion MRI (dMRI) is a similar MRI technique that images the diffusive motion of water molecules. As discussed in the previous section, the monitoring of this diffusion can reveal information regarding the underlying geometry of the cellular environment and thereby provide information about the physiological condition of the cellular landscape. Hence, dMRI has gained significant traction in the last three decades as a tool for the investigation of human anatomy and the diagnosis of various pathologies [8–10]. While not restricted exclusively to imaging the brain, from here onwards the discussions of dMRI and related methodologies will center upon neuroimaging applications.

1.3.1 Sensitizing MRI to Diffusion

The notion of using nuclear magnetic resonance (NMR) to monitor diffusion was initially suggested by Torrey [11], who developed a framework to integrate Fick’s law (Equation 1.1) into the Bloch equations as:

$$\frac{dM_t}{dt} = -i\gamma\vec{G} \cdot \vec{r} - \frac{M_t}{T_2} + D\nabla^2 M_t \quad (1.5)$$

Equation 1.5 is known as the Bloch-Torrey equation where M_t is the transverse magnetization, D is the diffusivity, γ is the gyromagnetic ratio, T_2 is the spin-spin relaxation time and $G(r)$ is a spatially dependent magnetic field gradient. Through this equation Torrey proposed that the magnetization of diffusing spins could be monitored through the application of a spatially varying local magnetic field gradient $G(r)$ [11]. Stejskal and Tanner later extended this framework [12] to use pulsed gradients that were feasible to implement in a technique that is now known as Pulsed Gradient Spin-Echo (PGSE) [13].

PGSE inserts two trapezoidal gradient pulses symmetrically on either side of the refocusing radiofrequency (RF) pulse in a conventional Spin-Echo sequence and in the years that followed this technique began to be applied *ex vivo* to monitor diffusion in various biological systems including human muscles [14] and different types of cells [15]. The solution to equation 1.5 describing the transverse magnetization can be written as [16]:

$$M_t = e^{-i\gamma \int_0^t \mathbf{G}(t') \cdot \vec{r} dt} \cdot e^{-t/T_2} \cdot e^{-D\gamma^2 \int_0^t (\int_0^\tau \mathbf{G}(t') dt')^2 d\tau} \quad (1.6)$$

This solution can be interpreted as having three parts (split as the 3 exponential terms): a complex phase term due to gradient dephasing effects, a term that describes the T_2 relaxation of the magnetization according to the Bloch equations and an additional term which attenuates the signal based on the diffusion induced dephasing during the gradients. This final term is of most interest and describes precisely how the MRI signal is made sensitive to diffusive movements.

As seen in the final term of equation 1.6, the diffusion gradient is the critical component to sensitize the acquired signal to diffusion. According to the Larmor equation:

$$\omega(\vec{r}) = \gamma(B_0 + G(\vec{r})) \quad (1.7)$$

the angular precession frequency of nuclear spins ω can be altered by applying a spatially dependent magnetic field gradient $G(r)$ which acts to modify the magnetic field experienced by the spins based on their position \vec{r} (i.e. can add or subtract from the main field B_0); this is the principle that enables the spatial localization of the MRI signal for image generation. This effect is scaled by the gyromagnetic ratio γ , which is a constant defining the precession frequency per unit magnetic field associated with the nuclear species (for H^1 , $\gamma = 2.675 \times 10^8 \text{ rad/s/T}$). Based on the solution to the Bloch-Torrey equation (equation 1.6) and through interpretation of the Larmor equation, the application of a magnetic field gradient will impart some additional phase on the signal (via the complex

phase term in equation 1.6). The introduction of this phase causes the spins to dephase relative to each other, leaving their presumed coherent state - this is the result of the application of the initial diffusion gradient. This change in coherence is precisely reversed by the effects of the second diffusion gradient which acts in the exact opposite manner (due to its placement after the refocusing pulse), to revert any dephasing accrued from the first gradient. Thus static (i.e. non-moving) spins will return to a coherent state before the signal is measured and thus the diffusion gradients in essence have no effect. However, for non-static spins that are moving (due to diffusion or otherwise) there is additional dephasing that occurs due the movement during the gradient pulse (see the third exponential term in equation 1.6). The spatial variation in magnetic field due to the gradient means that as any particular spin moves it experiences a slightly different magnetic field resulting in dephasing. This allows the gradients to, in effect tag the diffusing molecules by applying additional dephasing in a manner proportional to their displacement. This dephasing due to diffusion is not resolved by the second diffusion gradient and results in net signal loss via reduced echo amplitude. The reduction in the acquired signal is what is generally referred to as diffusion weighting. The effect of the diffusion gradients on both stationary and non-stationary spins is visualized in Figure 1.4.

It should be noted that this effect is true for all gradients in an imaging sequence and hence is not exclusive only to the diffusion gradients however, the magnitude and duration of the gradients required for diffusion encoding significantly dominate this effect; the diffusion weighting applied by a sequence that does not contain dedicated diffusion encoding gradients is typically 2-3 orders of magnitude lower and hence any effects of diffusion on the signal are negligible [7].

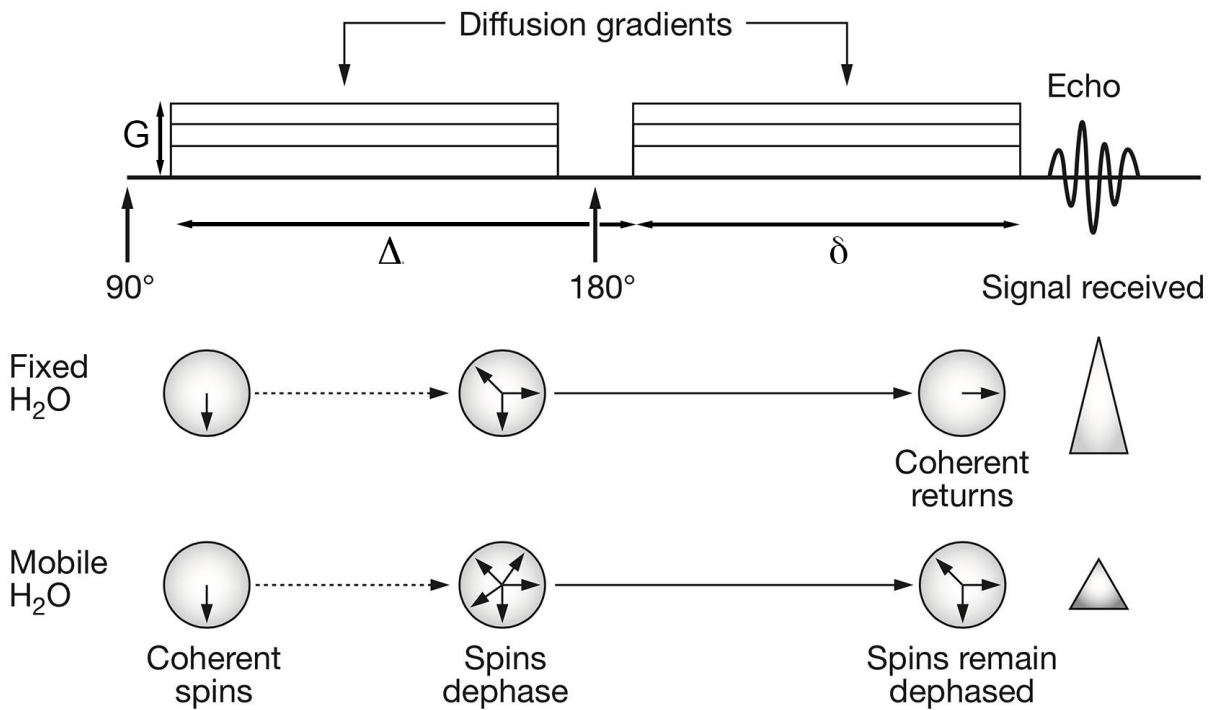


Figure 1.4: Spin dephasing behaviour for a typical diffusion sequence. Static spins experience dephasing due to gradients alone which is reverted by the second gradient. Diffusing spins experience additional dephasing due to thermal displacements which is not reverted by the second diffusion gradient resulting in signal loss. As shown δ corresponds to the gradient duration, Δ denotes the gradient duration plus the time which separates the two diffusion gradients and G denotes the gradient amplitude. Figure adapted from Patterson et al. [10]

1.3.2 Diffusion Attenuated Signal

Le Bihan *et al.* [17,18] were the first to aggregate these gradient-dephasing effects, lumping them into a single factor called the b-value. Moreover, the work by Le Bihan *et al.* [17] represented the first measurements of in vivo diffusion using MRI, pioneering the field from that point on. Adopting this convention allows the diffusion-attenuated portion of the signal to be written compactly as:

$$S(b) = e^{-D\gamma^2 \int_0^t (\int_0^\tau G(t') dt')^2 d\tau} = S_0 e^{-bD} \quad (1.8)$$

where D is the diffusivity, b is the diffusion weighting (b-value), S_0 is the signal with no diffusion weighting applied and $S(b)$ is the acquired signal. Based on equation 1.8 the b-value can be interpreted as the amount of diffusion weighting that is applied in an acquisition; to preserve dimensionality it has units of *time/length*². Practically the b-value gives an indication of the amount of signal attenuation that will occur in the image due to diffusion and is generally proportional to the square of the amplitude of the applied gradient. To illustrate this point, Figure 1.5 shows diffusion weighted images (DWIs) of a healthy human brain acquired with increasingly larger b-values using PGSE, demonstrating the increased signal attenuation with greater diffusion weighting.

For a pair of pulsed gradients as proposed by Stejskal and Tanner [12,13] and as used by Le Bihan *et al.* [17] the b-value can be written as:

$$b = -\gamma^2 G^2 \delta^2 \left(\Delta - \frac{\delta}{3} \right) \quad (1.9)$$

Where the definitions of δ , Δ and G in relation to the gradient pulse are illustrated in Figure 1.4. Hence, by controlling the gradient specifications, in particular gradient amplitude and duration, a broad range of diffusion weighting can be achieved. Diffusion encoding gradients can be applied along any one (or combination of) the three axes that

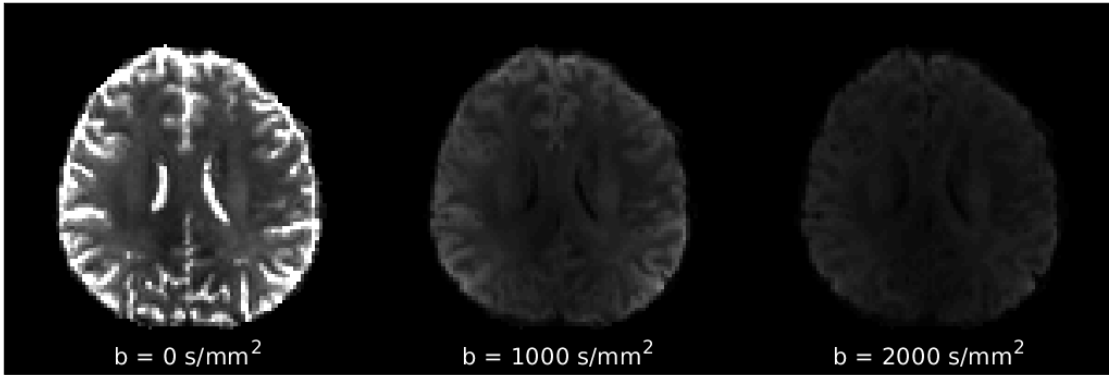


Figure 1.5: Diffusion weighted images (DWIs) acquired with PGSE at b-values of 0 (left), 1000 (middle) and 2000 s/mm^2 (right). Images demonstrate decreasing SNR due to increasing signal attenuation with larger b-values (moving from left to right).

compose the cartesian scanner coordinate system. Generally these are referred to as G_x , G_y and G_z for gradients applied along the x , y and z axes respectively.

Since the signal is attenuated as spins diffuse, dMRI suffers from inherently lower signal-to-noise ratio (SNR) than its parent proton MRI methods. As seen previously in Figure 1.5 the reduction in SNR is apparent for increasing b-value and hence this requires an increased number of averages to maintain the same SNR, thereby elongating the scanning time. Moreover applying diffusion encoding along multiple directions can also increase scan times leading to generally longer scans than more conventional non-diffusion sequences.

1.3.3 Apparent Diffusion Coefficient

The diffusivity that appears in equations 1.6 and 1.8 implies that the diffusion coefficient of the water molecules being tracked can be recovered by careful monitoring of the magnetization – which constitutes the signal, and knowledge of the gradients applied. However, while this may be feasible in NMR experiments, it is misleading to assume that the exact diffusion coefficient can be obtained from images where voxels sizes are on the order of a few millimeters while cell structures are on the order of microns. Instead, bulk

diffusion information is measured in each voxel, which is inclusive of additional effects that may influence measurements of diffusivity. These effects as observed by Le Bihan *et al.* [17] were termed intravoxel incoherent motion and include additional factors such as cardiac or respiratory pulsatile effects, microcirculatory or related flow and others. In this context the diffusivity is replaced with a more appropriate title known as the apparent diffusion coefficient (ADC). In current literature the term ADC is used to acknowledge both the presence of these effects in diffusion measurements and the inherent averaging of cellular diffusion effects within a single voxel. Nevertheless, this change in interpretation of the diffusivity as the ADC does not affect the method of its calculation. Based on equation 1.8, in order to calculate the ADC we require three values: b the b-value of the acquisition, $S(b)$ the measured signal with said b-value and S_0 the measured signal with no diffusion weighting applied. The b-value is known and selected as part of the scanning protocol and the signal S is acquired in each voxel constituting the image hence only S_0 remains unknown. For this reason common practice is to acquire two images in a diffusion protocol, one with the desired b-value and one with no diffusion weighting applied (though any two unequal b-values would suffice). Acquiring images at two different b-values permits the simple calculation of the ADC by fitting equation 1.8 to the curve generated from $S(b_1)$ and $S(b_2)$. To make this process more computationally efficient, a logarithm can be applied to equation 1.8 allowing it to be rewritten in the form of a straight line:

$$\ln(S(b)) = \ln(S_0) - bD \quad (1.10)$$

This allows the ADC to be extracted from a single parameter linear fit (see Figure 1.6) permitting an ADC to be determined for each voxel of the image. Displaying the ADC value of each voxel is known as an ADC map - an example of such a map is presented in Figure 1.7B. The contrast of ADC maps is inverted when compared to DWIs; in DWIs areas with higher ADCs appear darker while those with lower ADCs appear brighter. This can be understood by recalling the discussion from the previous section regarding

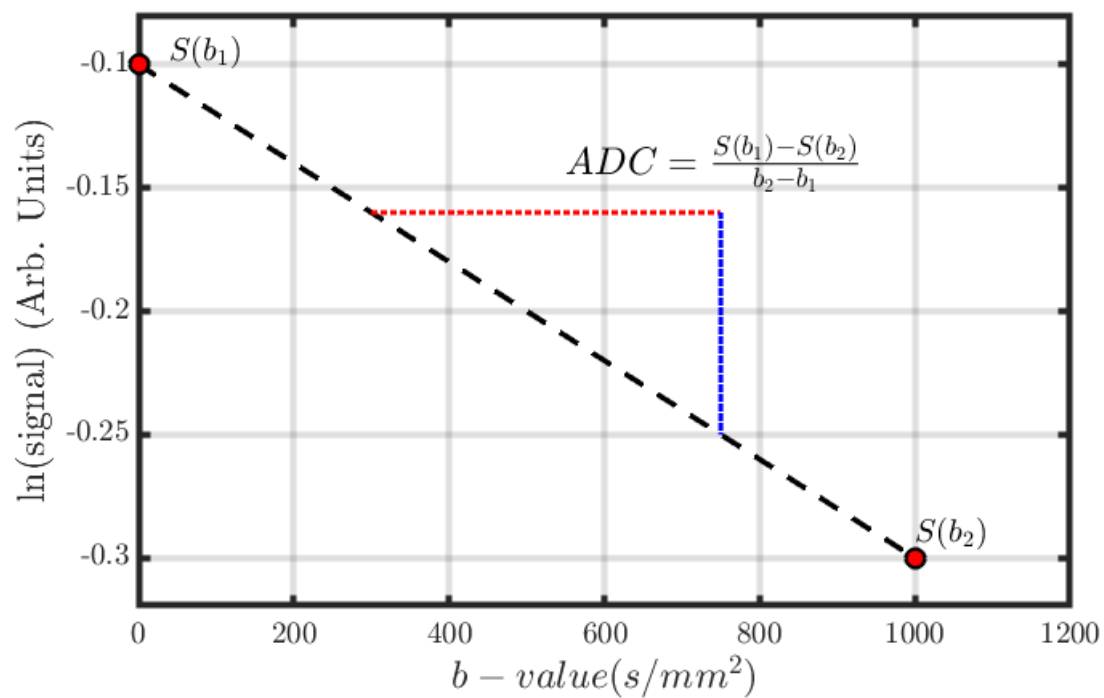


Figure 1.6: Typical diffusion signal curve generated from two b-value acquisitions corresponding to $S(b_1)$ and $S(b_2)$. The ADC is determined as the slope of the linear fit between the natural logarithm of the two points according to equation 1.10.

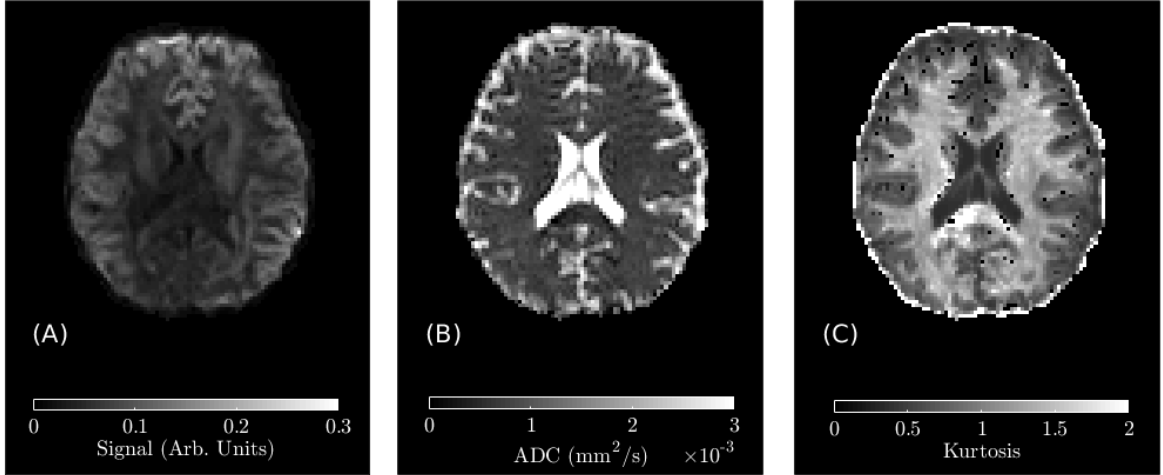


Figure 1.7: Comparison of various diffusion metrics and contrasts from a healthy subject. (A) DWI acquired with PGSE at $b = 1000 \text{ s/mm}^2$, (B) calculated average ADC map and (C) calculated apparent kurtosis map generated from $b = 0, 1000, 2000 \text{ s/mm}^2$ acquisitions.

the attenuation of the signal due to diffusion - namely that a larger ADC will result in a more attenuated signal. Figure 1.7 shows the distinct contrast in diffusion-weighted images with cerebrospinal fluid (CSF) in the ventricles appearing considerably darker than brain parenchyma due to the increased diffusivity of CSF.

As discussed previously in Section 1.2, anisotropic diffusion creates a directionally dependent diffusion coefficient based on cellular and/or environmental structures. Practically, this translates to a directionally dependent ADC which can be probed through the application of gradients along any one (or combination of) directions. Initially proposed by Basser *et al.* [19] diffusion tensor imaging (DTI) provides a formal framework to account for this directional dependence of the ADC. The dependence is conveyed through the diffusion tensor \mathbf{D} whose components comprise the measured diffusivity along each direction [20]. Traditionally the diffusion tensor is written as:

$$\mathbf{D} = \begin{bmatrix} D_{xx} & D_{xy} & D_{xz} \\ D_{yx} & D_{yy} & D_{yz} \\ D_{zx} & D_{zy} & D_{zz} \end{bmatrix} \quad (1.11)$$

where D_{nm} denotes the ADC measured along the n and m directions simultaneously. Since the tensor is both real and Hermitian it is also symmetric (i.e. that $D_{xy} = D_{yx}$, $D_{zy} = D_{yz}$, $D_{xz} = D_{zx}$) therefore only six of the nine elements are unique. Consequently at least six diffusion directions are required to calculate the entire tensor (not including the necessary $b = 0$ acquisition) [21]. While six is the minimum number of non-collinear directions required to estimate \mathbf{D} , additional directions provide increased sensitivity to complex fibre arrangements (e.g. crossing or kissing fibres) [22] and may reduce sensitivity of tensor metrics to noise [23].

From \mathbf{D} , it is also possible to derive numerous metrics and maps including the fractional anisotropy (FA), which enables the visualization of anisotropy, radial and axial diffusivity (RD, AD) that describe the diffusion in radial and axial directions relative to the orientation of the neurite and mean diffusivity (MD), which is the average diffusivity along the x , y and z directions.

The utility of DTI and its associated key metrics is undisputed; since its introduction it has quickly become the Gold Standard for investigating in vivo diffusion with MRI and has found a myriad of clinical and research applications. These applications, though too broad to discuss in detail here, include the detection and monitoring of cerebral ischemia, multiple sclerosis lesions, Alzheimer’s disease, epilepsy and various types of tumors and tumor associated edema [24, 25].

1.3.4 Diffusion Kurtosis

The utility of ADC measurements and DTI protocols are undisputed; however, despite this, these methods remain beneath the assumption that measured diffusion is Gaussian. While this may be the case for free diffusion where predictions from Einstein remain valid, this assumption breaks down for intricate cellular environments where membranes and other obstacles act to restrict diffusion (as discussed in section 1.2). The result is a deviation from the Gaussian distribution to reflect the presence of such barriers. The

kurtosis is a statistical measure that serves to quantify this degree of non-Gaussianity. In the context of diffusion, a positive kurtosis reflects a narrowing of the probability distribution as shown in Figure 1.8 and is associated with restricted diffusion through a reduction of the MSD.

Practically, the kurtosis is introduced through a series expansion of the signal $S(b)$ and results in an additional second order term added to equation 1.8 [26, 27]:

$$S(b) = S_0 e^{-bD + \frac{b^2 D^2 K}{6}} \quad (1.12)$$

where K denotes the dimensionless kurtosis and all other parameters remain the same as in equation 1.8. Equation 1.12 can be understood as having an additional higher order term which acts to correct the signal for large b -values where the linearity of equation 1.10 breaks down due to the assumptions discussed (see Figure 1.9). Consequently, the kurtosis is only apparent for high diffusion weighting ($b > 1000 \text{ s/mm}^2$) where the nuances of cellular barriers become evident. In practice this makes kurtosis imaging more demanding on scanner hardware than traditional diffusion sequences requiring high gradient amplitudes and longer gradients to achieve necessary b -values though even still, kurtosis imaging is well within reach of most clinical systems.

Similar to DTI an analogous treatment for kurtosis was also proposed [26] known as diffusion kurtosis imaging (DKI). Like DTI, DKI scales the signal in equation 1.12 up to 3-dimensions to capture the directionality by introducing a diffusion kurtosis tensor. Unlike the diffusion tensor however, the kurtosis tensor has 15 unique elements and thus requires at least 15 different directions to estimate. Despite their different definitions the kurtosis is obtained through a similar procedure as the ADC (ie. by fitting the signal curve). However, since this procedure now involves a two-parameter quadratic fit (equation 1.12 now contains a b^2 term), at least 3 b -values are required to determine both the ADC and the kurtosis from acquired data.

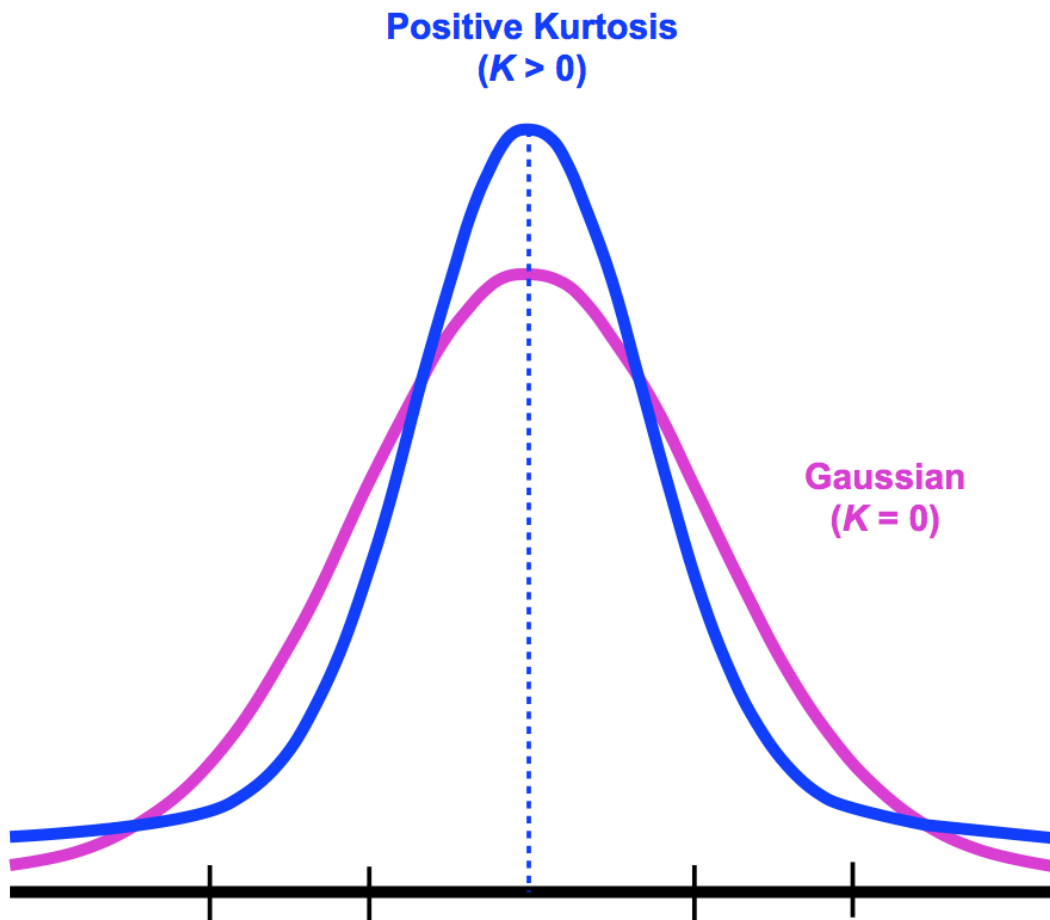


Figure 1.8: Probability distributions that governs the likelihood of a spin diffusing a given distance in a fixed time interval, for both zero kurtosis (pink) and positive kurtosis (blue). The narrowing of the probability distribution for positive kurtosis signifies restricted diffusion and increased heterogeneity compared to purely Gaussian diffusion which has no kurtosis. Image courtesy of Allen D. Elster, MRIquestions.com

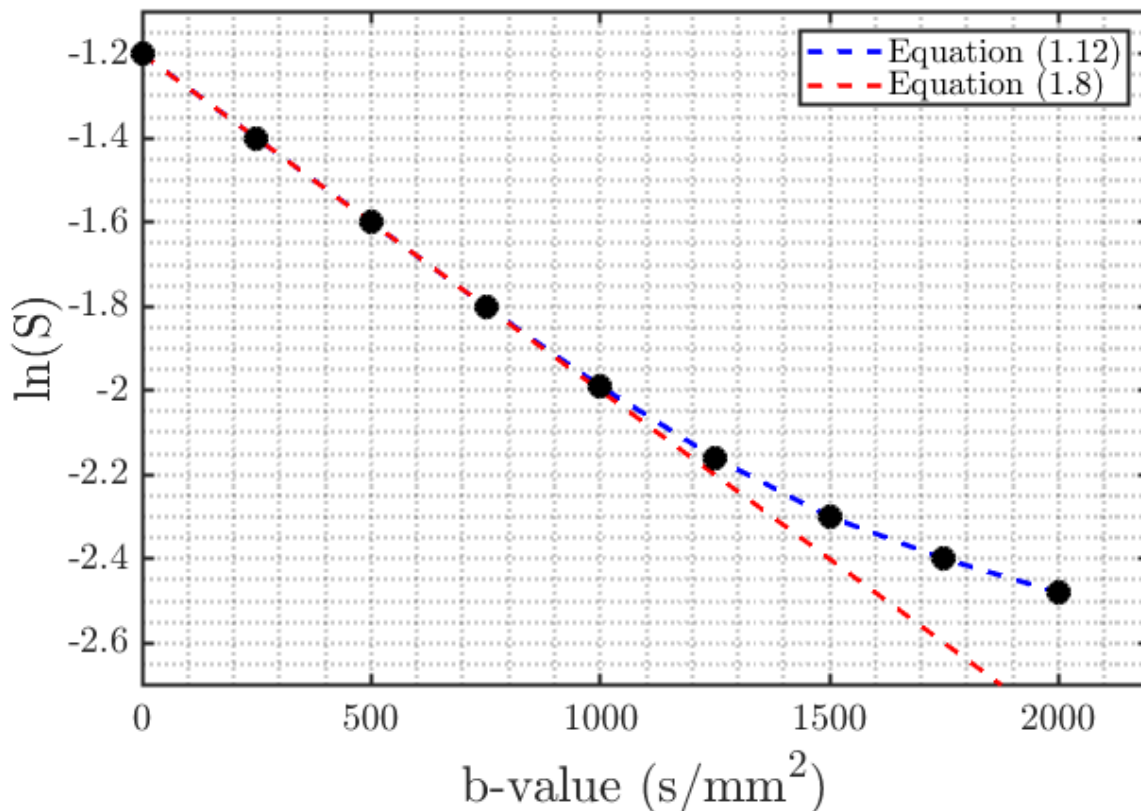


Figure 1.9: Natural logarithm of the diffusion signal across a wide range of b-values. The linear approximation of equation 1.8 is valid up to $b \sim 1000 \text{ s/mm}^2$. Higher order effects are observed for $b > 1000 \text{ s/mm}^2$ where the signal begins to deviate from the first-order linear approximation due to kurtosis effects and is better described by the additional term in equation 1.12.

Since its relatively recent introduction [26], kurtosis imaging has already demonstrated unique properties that have brought it to the forefront of diffusion MRI investigations. As seen in Figure 1.7C, kurtosis images display unique contrast between WM and GM demonstrating sensitivity to structural anisotropy that is not apparent from the ADC alone [26]. As a result significant clinical applications in neuroimaging have emerged. Recent progress in kurtosis imaging applications includes using kurtosis for the detection of ischemic and traumatic brain injury, Alzheimer’s disease, cognitive impairment and gliomas [28]. Moreover, despite the prominence in neuroimaging, kurtosis also has demonstrated utility in imaging pathology of other organs including the kidneys, breast, neck and prostate [28, 29]. Given its unique role recent efforts have focused on determining the optimal parameters for acquiring kurtosis images including the number of directions, target b-values and the distributions of said b-values with respect to each other [30–35]. Current work appears to focus on further optimizing acquisitions to generate higher SNR, reduce scan times and explore novel clinical applications.

1.4 Oscillating Gradient Diffusion MRI

The motivation for oscillating gradients stems from the notion that in the context of restricted diffusion the diffusion time (which can be thought as analogous to the exposure time of a camera), will determine the measured value of the ADC in a manner that reflects the surrounding geometry. As the effective diffusion time (t_d) is reduced, molecules probe increasingly shorter distances and thereby experience fewer interactions with boundaries, barriers and other cellular-level obstacles. In this sense the probing of shorter diffusion times can be understood as the probing of the transition from restricted to free diffusion; given a short enough amount of time to diffuse the molecule will not reach the boundary that would restrict its movement thus giving the appearance of free, isotropic diffusion. The result is an ADC that will be determined based on the diffusion time, with shorter

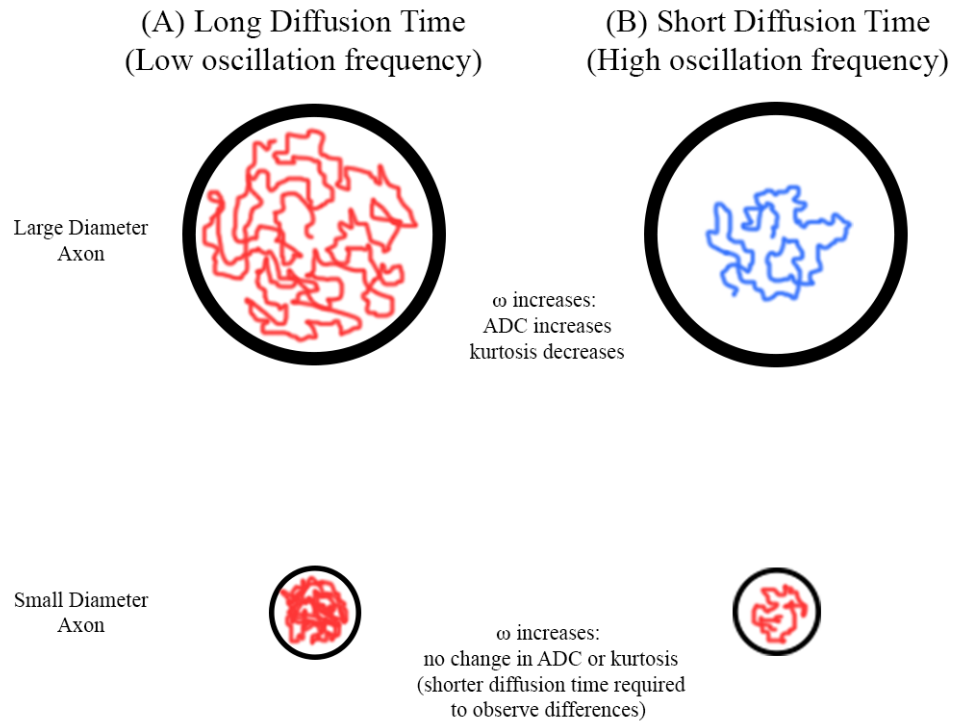


Figure 1.10: Visual representation of possible random walk trajectories for two relative diffusion times (or conversely two different oscillation frequencies) for both large (top row) and small (bottom row) diameter axons. Red trajectories indicate restricted diffusion, where the diffusion time is long enough to permit the boundary to limit the MSD resulting in reduced ADCs and increased kurtosis. Blue trajectories indicate free unrestricted diffusion resulting in larger ADC values and reduced (or zero) kurtosis. Since the distance to the boundary is less for smaller axons, an even shorter diffusion time would be required to observe differences in the ADC and kurtosis based on changes in the MSD, hence restricted diffusion is implied in small axons for both diffusion times.

diffusion times predicted to result in larger ADC values. This is represented graphically in Figure 1.10, demonstrating the effect of diffusion time on molecular movement, the ADC and the impact of cellular dimensions on this effect.

Recalling equation 1.3 it can be estimated that in 30 ms (a typical diffusion time for PGSE) a water molecule would diffuse $\sim 13 \mu m$ in any single direction. Given the distribution of axon sizes in the human brain varies between $0.5-10 \mu m$ in diameter [3] this diffusion time is insufficient to probe the length scales of individual axons. Consequently, such a measurement can only reveal a portion of the present microstructural features that

could otherwise be accessible through shorter diffusion times. While PGSE is limited to diffusion times greater than ~ 20 ms due to hardware constraints, oscillating gradient diffusion MRI provides a convenient method for reducing the diffusion time below that which is possible with PGSE. In doing so it provides a method for probing shorter length scales granting access to previously inaccessible microstructural characteristics. The mechanism of oscillating gradients, its current applications and limitation are discussed in more detail in the following subsections.

1.4.1 Oscillating Gradient Spin-Echo (OGSE)

The current implementation of oscillating gradients is known as oscillating gradient spin-echo (OGSE). Initially proposed by Gross and Kosfeld [36], Stepisnik later used a density matrix framework to derive an expression for the diffusion-attenuated signal of a time varying gradient as [37,38]:

$$S = S_0 \cdot \exp\left(\frac{-1}{2\pi} \int_{-\infty}^{\infty} F(\omega)D(\omega)F^*(\omega)d\omega\right) = S_0 \cdot \exp\left(\frac{-1}{2\pi} \int_{-\infty}^{\infty} |F(\omega)|^2 D(\omega)d\omega\right) \quad (1.13)$$

where S_0 is the signal without any diffusion weighting applied (i.e. $b = 0$ s/mm²), $|F(\omega)|^2$ is the gradient-modulation power spectrum and $D(\omega)$ is the diffusion spectrum which determines the frequency dependent diffusivity and can be derived from the velocity autocorrelation function [38]. The gradient modulation spectrum is constructed from an intermediate term $F(\omega)$ which is defined as:

$$F(\omega) = \int_{-\infty}^{\infty} \left(\int_0^{\tau} g(t)dt \right) e^{-i\omega\tau} d\tau \quad (1.14)$$

and can be interpreted as the Fourier transform of the zeroth moment of the gradient $g(t)$, corresponding to the phase accumulation of the spins. In order to acquire meaningful spectra (i.e. that have non-zero spectral components), periodic modulation of the diffusion gradient is required, where the modulation frequency is denoted as ω . This

modulation can take the form of sine or cosine apodization however, with sine modulation measuring diffusion at a particular non-zero frequency can be problematic as a sine function inherently produces a peak frequency at zero ($\omega_{peak} = 0$). Cosine modulation provides increased spectral selectivity by ensuring the peak frequency is non-zero ($\omega_{peak} \neq 0$) allowing specific frequencies to be probed. Additionally, the increase in maximum possible b-value between cosine and trapezoidal-cosine modulated waveforms is significant [39] and for this reason most modern implementations rely on the trapezoidal-cosine method. For this configuration the b-value can be calculated as [40]:

$$b = -\gamma^2 G^2 (t_r + t_p)^2 (\Delta - (t_r + t_p)/3 + t_r^3/30 - t_r^2(t_r + t_p)^2/6) \quad (1.15)$$

Where G is the maximum gradient amplitude, t_p is the period of the waveform (defined as $2\pi/\omega$) and t_r is the gradient rise time. However, the oscillatory nature of the gradient prevents the max amplitude from being exploited for the entire gradient duration and as a result the b-values are significantly lower for OGSE compared to PGSE (this limitation is discussed further in section 1.4.3). Figure 1.11 compares the gradient waveforms and power spectra of PGSE to both trapezoidal sine and cosine OGSE highlighting the key spectral differences.

Another key difference between PGSE and OGSE is the estimation of t_d , the effective diffusion time. While the t_d for PGSE (in the narrow pulse limit) can be calculated as $t_d = \Delta - \delta/3$, the effective diffusion times of OGSE sequences are not as well defined; the literature demonstrates disagreement on the exact relation of the diffusion time to oscillation frequency [40]. The initial solution was to use $t_d = 1/(4f)$, where $f = \omega/(2\pi)$ [41, 42] however later it was suggested a more accurate representation is $t_d = 7/(64f)$ [43]. Nevertheless, what is agreed upon is that the use of increasingly higher frequencies translates to shorter effective diffusion times, scaling inversely with frequency. For this reason it can be instructive to work instead in the spectral domain with reference to

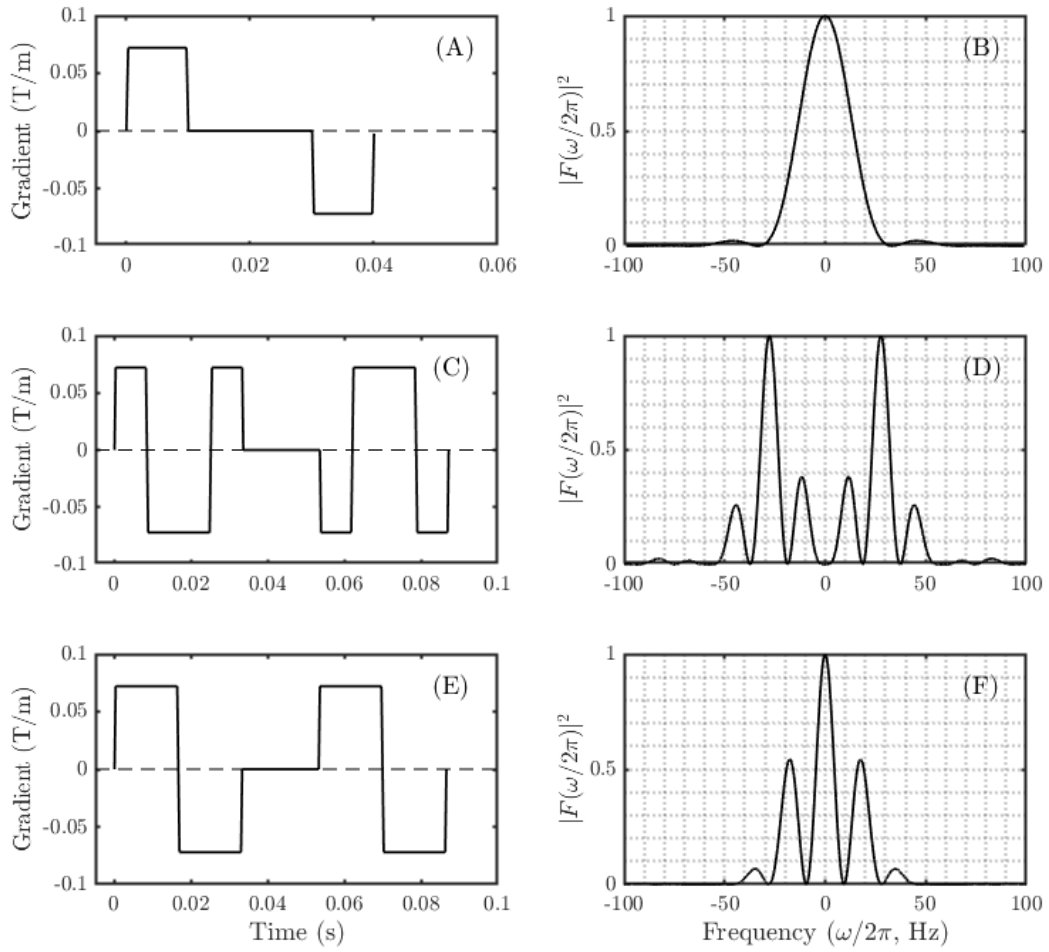


Figure 1.11: Comparison of gradient waveforms for PGSE (A), cosine modulated OGSE (C) and sine modulated OGSE (E). The corresponding normalized gradient modulation spectra are also shown (B,D,F) with cosine modulated demonstrating a non-zero peak frequency corresponding to the oscillation frequency. Waveform polarity is reversed for the second diffusion gradient due to the effects of the refocusing RF pulse (not shown); OGSE waveforms are shown using only 2 periods.

oscillation frequency as opposed to diffusion time. An increasing number of studies are adopting this approach [39, 44–46] as it eliminates the ambiguity of the diffusion time definition while still enabling time-dependent diffusion observations.

In essence OGSE enables access to shorter effective diffusion times by rapidly tagging and untagging molecules via phase accrual through the rapidly changing polarity of the gradient. This enables the exploration of time-dependent effects of diffusion that are otherwise invisible to PGSE and constitutes a unique tool for imaging diffusion in the brain.

1.4.2 Applications and Current Progress

Given the unique spectral treatment of diffusion enabled by OGSE, current applications revolve around probing the diffusion spectrum $D(\omega)$ to acquire frequency dependent ADC measurements. Due to advanced hardware capabilities that permitted easier implementation of OGSE, small animal studies were the first to explore time-dependent effects with oscillating gradients; in the following subsection, key studies from animal subjects are summarized followed by recent progress in human imaging and an examination of current avenues of interest.

Initial investigations of the time-dependent ADC were conducted in healthy and ischemic rat brains by Does *et al.* [41] who demonstrated an ADC increase with frequency. Subsequent works built upon this study applying OGSE to mouse models and demonstrating increased sensitivity to gliomas [47, 48] and ischemic injury [45, 49, 50] compared to PGSE alone. From these studies evidence was presented demonstrating the ability to differentiate between diseased and healthy tissue based on the response of the ADC measured across varied frequency.

During this time advances were also made in connecting short diffusion time ADC measurements with quantitative microstructural properties. The effect demonstrated in Figure 1.10 also intuitively suggests some sensitivity to cell dimensions. Using a fixed

diffusion time, larger changes in ADC would be expected for larger diameter axons for example. Hence theoretical frameworks were developed to enable the determination of surface-to-volume ratios [51], extracellular space [52] and mean cell size [53–56]. Of particular note, the concept of temporal diffusion spectroscopy [57–59] which uses OGSE for the determination of cell sizes has recently received significant attention, with numerous studies demonstrating the ability to infer tumor and cell sizes in both human and animal models [53, 56, 60–64].

In addition to ADC investigations recent studies by Wu *et al.* [45] and Aggarwal *et al.* [65] have demonstrated OGSE measurements of in vivo kurtosis with mice. While previous studies have observed time-dependent kurtosis ex vivo using prepared samples of porcine spinal cord [66] and small animal brains [67, 68], the studies of [45] and [65] constitute the first (and at the time of writing the only) published studies to image the diffusion kurtosis in vivo using OGSE. The findings from both studies suggest a non-monotonic behavior of the kurtosis when measured across a wide range of diffusion times. This is in agreement with ex vivo observations and can be understood by considering cellular exchange. The longer exchange times predicted by the Kärger model of exchange are typically shorter than the effective diffusion times attainable with OGSE [69, 70], as a result the kurtosis is expected to decrease with frequency as diffusion becomes increasingly Gaussian. The longer diffusion times of PGSE make the measured diffusion susceptible to exchange effects, which cause the kurtosis to decrease with diffusion time. Notably, Aggarwal *et al.* [65] also present simulations that suggest permeability plays a role in time-dependent kurtosis metrics which also explains the sensitivity of their measurements to detecting demyelination.

Due to the gradient hardware limitations of clinical MRI systems, only a handful of studies have successfully implemented OGSE imaging in the human brain. The pioneering studies of [42] and [39] were the first to demonstrate the use of oscillating gradients for in vivo measurements of diffusion. Results from DTI studies performed by Baron and

Beaulieu [42] confirmed the findings from previous small animals studies indicating that through the reduction of effective diffusion time OGSE provides additional sensitivity to diffusion that is not observable with PGSE. Notably, Van *et al.* [39] were the first to demonstrate the superiority of using trapezoidal cosine-modulated gradients for improved OGSE diffusion encoding, citing better spectral selectivity and increased b-value. Studies have since continued to explore the time-dependent ADC and its utility for detection of ischemic injury [71, 72], benign and malignant tumors [73] and cell size measurements [53, 56, 60–64].

Moreover, recently Arbabi *et al.* [44] demonstrated the frequency dependence of the ADC (termed diffusion dispersion) takes the form of $D(\omega) \propto \omega^{1/2}$. This key result also validates the predicted structural disorder model proposed for neurites [74] and is one of the first studies to quantitatively assess a time-dependent microstructural model in the human brain using OGSE. Moreover, [44] also demonstrated the acquisition of so-called diffusion dispersion maps, whose contrast is based on the difference in ADC values (ΔADC) between PGSE and OGSE acquisitions (or conversely between a long and short diffusion time). Investigations using these diffusion dispersion maps have recently proved useful in the assessment of ischemia in neonates [75], the differentiation of malignant from benign tumors [73] and structural changes in conditions such as Down Syndrome [76]. In addition to these studies recent measurements from Tétreault *et al.* [77] have used OGSE to characterize time dependent diffusion in the corpus callosum of the human brain finding preliminary dependencies on both sex and age across healthy subjects.

The utility of OGSE is still being realized with an increasing number of clinical and research studies employing the technique. Current and future work focuses on improving acquisition times, incorporating higher performing gradients and improved time-dependent microstructural models.

1.4.3 Limitations

Briefly discussed above, the primary limitation of OGSE methods is the limited parameter space available for protocol (and thereby study) design. This is apparent through the significant technical restriction of two key acquisition parameters: the b-value and the echo time (TE).

The periodic modulation of the diffusion gradient ensures only gradient waves can be implemented where the duration of the wave is dependent on the frequency and number of oscillation periods, N (see Figure 1.12). This causes the diffusion gradient durations to be longer than those typically required for PGSE. This effect is particularly sensitive to the selected frequency, with lower frequencies requiring increasingly longer TEs due to the longer period of the waveform. The result is intrinsically longer TE values associated with OGSE sequences. Studies in the human brain typically have $TE > 110$ ms causing exponential signal loss due to T_2 decay; for comparison the typical TE of PGSE based diffusion sequences lay in the range of ~ 60 -80 ms. For this reason partial Fourier phase encoding (which is often employed for PGSE as well) is especially advantageous for the readout of OGSE images. This technique exploits the conjugate symmetry of k-space acquiring only a fraction of the entire space. Partial Fourier encoding reduces the readout of the sequences effectively resulting in shorter echo times and reduced scan time both of which are much desired for OGSE.

The second limitation occurs again due to the oscillating nature of the diffusion gradients. Modulation prohibits the maximum gradient amplitude from being exploited for the entire gradient duration as is possible with PGSE (see Figure 1.12). As a result, the b-values associated with cosine-modulated OGSE gradient waveforms scale inversely with frequency according to the relation $b \propto 1/f^3$ [40]. Hence, higher frequencies are severely limited by the range of b-values that can be accessed. Moreover, while the addition of more periods can mitigate this effect by enabling longer gradient wave-trains, these simultaneously act to further elongate the TE of the acquisition. As a result, previous

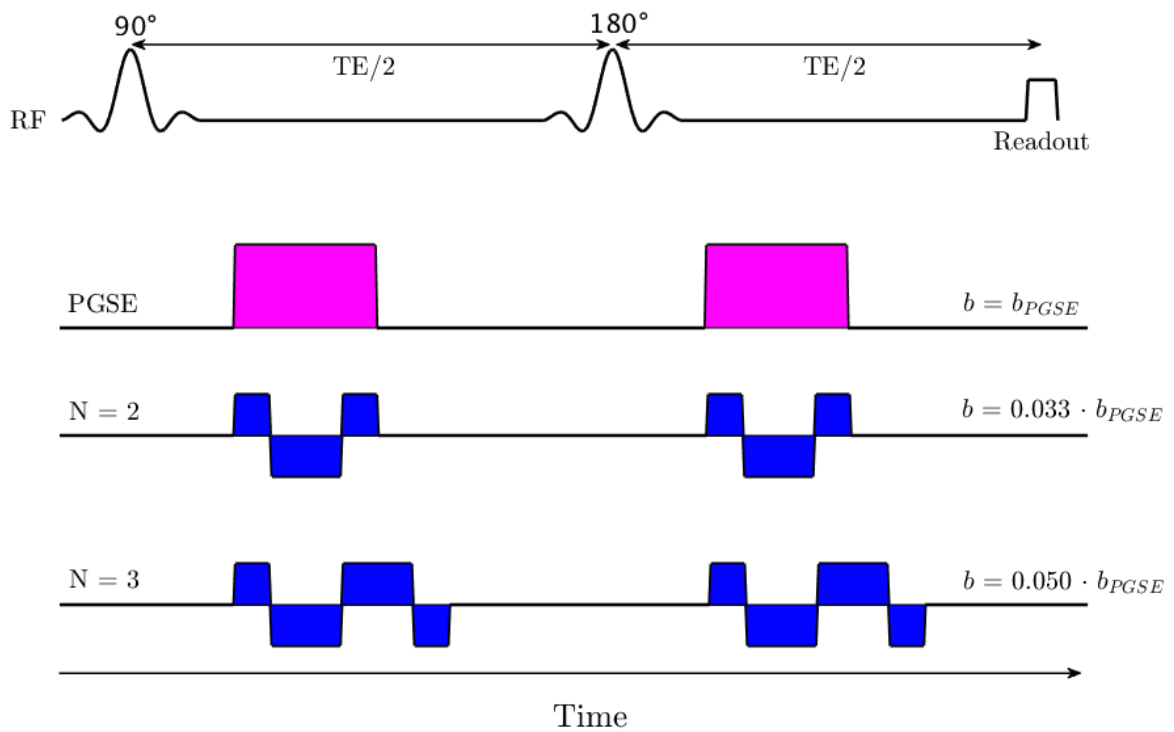


Figure 1.12: Comparison of PGSE with 40 Hz $N = 2$ and $N = 3$ cosine modulated trapezoidal OGSE. For the same gradient amplitude and slew rate, $N = 2$ OGSE can achieve only $\sim 3\%$ of the b-value possible with a PGSE sequence of equal duration (b_{PGSE}). Increasing the number of oscillation periods (N) can increase the b-value, however addition of extra periods also elongates the gradient duration as shown for $N = 3$.

studies conducted in the human brain have relied on either low b-values ($b < 500 \text{ s/mm}^2$) or have limited frequency ranges (typically 20-60 Hz). In an effort to achieve larger b-values it is becoming increasingly common to utilize a 4-direction tetrahedral direction scheme, where the diffusion gradients are applied along the four directions constituted by the vertices of a tetrahedron. While this is an insufficient number of directions to compute a full diffusion tensor, it does have the compelling advantage of enabling access to higher b-values, increasing the max b-value by 50% compared to a 6-direction scheme. As outlined by Conturo *et al.* [78] because the tetrahedral scheme samples all 3 principal directions (x,y,z) simultaneously it enables the gradients along each direction to be maximized at the same time, achieving larger maximum b-values. A separate emerging solution to this issue is the use of high-performance gradient systems [79–81] which have expanded the parameter space considerably to include studies with b-values in excess of 900 s/mm^2 [82] and oscillation frequencies up to 100 Hz [83]. The larger gradient amplitudes (up to 200 mT/m) and slew rates (up to 500 T/m/s) permit significantly higher b-values to be achieved than on clinical systems where gradient amplitudes are typically 60-80 mT/m. Larger gradient amplitudes however, increase the concerns regarding peripheral nerve stimulation (PNS) in which the rapidly changing magnetic field gradient induces stimulating electrical current in nerves resulting in involuntary muscle contractions. While less concerning for neuroimaging with head only scanners, this consequence remains for full body scanners where the PNS threshold is lower and must be considered for OGSE protocol design, particularly when high frequencies ($f > 60 \text{ Hz}$) or exceptional gradient amplitudes are to be used.

In addition to echo-planar imaging (EPI) and k-space related artifacts that affect PGSE diffusion MRI, OGSE also suffers from particularly strong eddy current distortions and artifacts. The rapid switching of the gradient polarity that occurs with OGSE induces the formation of strong eddy currents in conductive hardware components via Faraday’s law. The induced currents act to alter the local magnetic field thereby contributing to

magnetic field inhomogeneity. The result is distortions in acquired DWIs in the form of shearing, stretching, scaling and/or positional shifting artifacts [84]. Strategies have evolved for mitigating eddy current effects including gradient waveform compensation [85] and acquiring reverse polarity gradients [86]. Recent work on this front has worked to characterize time-varying eddy currents using retrospective model-based correction algorithms [87] however, the gold standard for eddy current correction is accomplished through the use of advanced field-monitoring systems. These systems consist of several probes that function to directly measure local changes in field homogeneity during the imaging sequence and as a result have the unprecedented ability to precisely correct for eddy current induced distortions and artifacts. Their use in this work and in other studies constitutes a vital tool in the enhancement of diffusion weighted image quality.

1.4.4 Summary

OGSE provides a method for achieving diffusion times that are substantially shorter than what is possible with PGSE methods by modulating the diffusion gradient at a frequency ω . This results in OGSE providing microstructural diffusion information on shorter length scales associated with increasing frequency, leading to observations of frequency dependent ADCs. The investigation of the frequency/time dependent ADC is still on going but select recent findings, in both animals and humans, have already demonstrated key applications in probing tissue microstructure and exploring pathology through the frequency dependent ADC. Despite these advances however, numerous technical challenges still exist in the implementation of OGSE sequences on human scanners. Together, the restrictions of the b-value and the long TEs continue to limit the applications of OGSE in both clinical and research settings. The careful balancing of b-value, frequency and TE has made protocol design with OGSE substantially more difficult than using PGSE methods alone. In the context of this work, these limitations have also contributed to the lack of studies exploring the frequency-dependent kurtosis in vivo. This

thesis sets to address this unexamined area by presenting the first measurements of the frequency dependent kurtosis in the human brain using a clinically relevant gradient system.

Chapter 2

Bipolar oscillating gradients for mapping diffusion kurtosis dispersion in the human brain

2.1 Introduction

Conventional diffusion MRI is performed using the well characterized pulsed gradient spin-echo (PGSE) sequence [12]. PGSE sequences enable efficient generation of diffusion weighting, and recent studies have explored time-dependent diffusion using PGSE methods [70, 88]. However, due to hardware limitations the range of accessible diffusion times remains limited to $> \sim 20$ ms.

Complimentary to PGSE, oscillating diffusion gradients initially proposed by Stepnik [37, 38], are utilized in oscillating gradient spin-echo (OGSE) sequences. While the effective diffusion time is not well defined for oscillating gradients, it is generally accepted that shorter effective diffusion times can be achieved with increasing oscillation frequency ω when compared to PGSE [40–42]. Consequently, OGSE has constituted a powerful tool in the investigation of time-dependent restricted diffusion through mon-

itoring of the ADC. As ω is increased, tracked water molecules diffuse shorter lengths and thereby have a reduced capacity to probe the surrounding environment; hence, the apparent diffusion coefficient (ADC) approaches the free diffusion limit. Deviations from this intrinsic limit, manifested as reductions in the ADC, can be instructive in providing information about physiological structures impeding diffusion such as cell membranes, cell density or extracellular components. Recent applications on this front include the probing of cell dimensions [53, 55, 60, 63, 64, 89], surface-to-volume ratios [51, 90] and additional microstructural characteristics such as packing [58, 91], extracellular space [52] and pore sizes [58]. Recently, OGSE sequences utilized by Arababi *et al.* [44] have also been used to investigate structural disorder in the human brain, confirming the predicted square-root dependence of the ADC on oscillation frequency [74].

It must be noted that most ADC investigations and diffusion tensor imaging (DTI) protocols fundamentally rely on Gaussian diffusion approximations [7]. However, local inhomogeneity of the tissue microenvironment results in deviations from Gaussian diffusion. Such deviations are quantified by extending the DTI treatment to estimate the directionally dependent diffusion kurtosis tensor, formally introduced in diffusion kurtosis imaging (DKI) [26, 92]. Similar to the ADC, it has been proposed that the diffusion kurtosis is also a time-dependent quantity, approaching zero with vanishing effective diffusion times [27]. Studies by Lee *et al.* [70] have used PGSE to explore time-dependent kurtosis in human gray matter, while small animal studies [65, 68, 88, 93] in addition to *ex vivo* studies [66, 67] have benefited from advanced hardware to observe time-dependent kurtosis more thoroughly. Notably, Aggarwal *et al.* [65] used both PGSE and OGSE methods to characterize the time-dependence of diffusion kurtosis in mice while Wu *et al.* [93] demonstrated the use of OGSE kurtosis imaging of healthy and injured mouse brains. Moreover, both studies highlight the utility of comparing kurtosis measurements between PGSE and OGSE in the form of difference maps, indicating their sensitivity to demyelination [65] as well as hypoxic-ischemic injury [93].

Despite this however, at the time of writing only a single recent preliminary work by Yang et al. [94] has explored the in vivo kurtosis in the human brain using oscillating gradients. The technical challenges associated with translation to clinical imaging systems have severely limited kurtosis measurements in humans using OGSE. In particular, limitations of gradient systems (both slew rate and gradient amplitude) have significantly hindered progress on this front by restricting the range of frequencies and b-values available for protocol design. The recent advent of high-performance gradient insert coils (as used by Yang et al.) has expanded this parameter space and made kurtosis measurements more feasible. Such gradient insert coils significantly outperform modern clinical gradient systems, routinely realizing max amplitudes of 200 mT/m and slew rates in excess of 500 T/m/s [80,94,95] permitting both rapid slewing and increased gradient amplitudes to be achieved across a wider range of frequencies [83]. Unfortunately, such hardware is not widely accessible and thus there remains a need to accommodate kurtosis measurements with OGSE to clinically relevant systems to further explore its utility for investigating restricted diffusion.

In this work we demonstrate the first kurtosis measurements in humans using OGSE with a clinically relevant gradient system. Our measurements, in conjunction with PGSE acquisitions, enable the generation of maps demonstrating the frequency dispersion of both the ADC and the diffusion kurtosis. This protocol is enabled by a novel gradient waveform design that reduces the echo time (TE) of the diffusion gradient while retaining the intrinsically high b-values required for kurtosis imaging. In the sections that follow we present our waveform design, the optimization and validation of our acquisition protocol and preliminary results for diffusion kurtosis dispersion in healthy human subjects.

2.2 Methods

2.2.1 Gradient Waveform Design

Conventional OGSE is typically performed with trapezoidal cosine modulated waveforms (Figure 2.1B) to maximize the achievable b-value [39]. However, recently proposed by Hennel et al. [82], the conventional cosine sequence can be modified by optimizing ramp times and reducing the spacing between the two diffusion gradients to the minimum allowable, thereby effectively consolidating the two diffusion gradients into a single waveform. These changes were shown to produce more selective power spectra and increased diffusion weighting capabilities [82]. The framework presented by Hennel et al. enabled the implementation of a non-integer number of periods introducing the $N = 2n + 1/2$ convention where N constitutes the number of periods and n is an integer greater than 0.

Our proposed waveform achieves shorter diffusion weighting durations by utilizing only $N = 1.5$ net oscillation periods over both sides of the refocusing RF pulse via two bipolar gradient waveforms that are tuned to achieve the desired net frequency. This approach functions to reduce the duration of the diffusion gradients and thereby significantly reduce the TE of the acquisition. A comparison between this new $N = 1.5$ waveform and normal $N = 2$ cosine modulated OGSE is presented in Figure 2.1, where similar spectral selectivity is demonstrated between the two methods.

The waveform is constructed by initially determining duration of the second lobe (T) using the expression:

$$T = \frac{1}{2} \left(\frac{1}{f} - \tau_{RF} - 2\tau \right) \quad (2.1)$$

where τ_{RF} is the separation required for the refocusing pulse and τ is the gradient rise time. This equation stems from an assumption that the central lobe of the three lobe k-space waveform will dominate the net frequency content of the diffusion weighting (see middle column of Figure 2.1). Constraining the integral of the zeroth moment to be zero

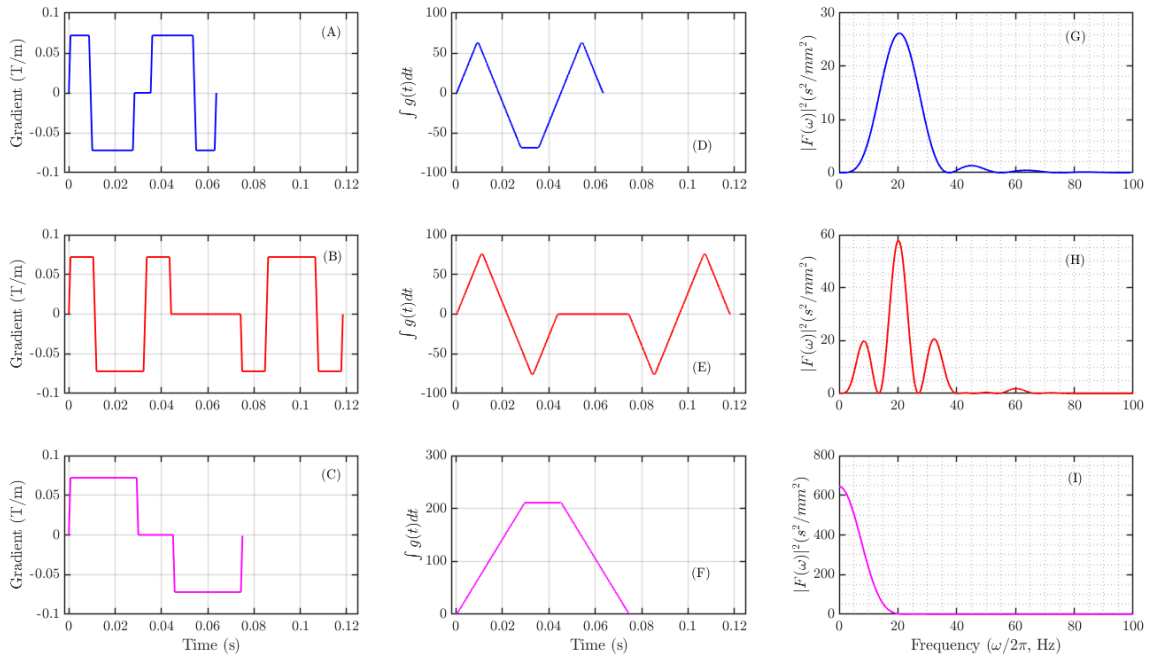


Figure 2.1: Comparison of new bipolar $N = 1.5$ OGSE waveform (A), $N = 2$ OGSE (B) and PGSE (C) waveforms. Corresponding power spectra (G-I) are also shown demonstrating comparable spectral selectivity between $N = 1.5$ and $N = 2$ OGSE for the target frequency. Also shown is the zeroth moment of each waveform (D-F). Continuous periodicity of the zeroth moment is apparent in the $N = 1.5$ waveform (D) compared to $N = 2$ (E) due to the reduction of the gradient separation time.

to eliminate any DC spectral components, the duration of the first lobe (L) can then be calculated as (see Appendix A):

$$L = \frac{1}{2} \left(-2T - \tau_{RF} - 7\tau + \sqrt{8T^2 + 8T\tau_{RF} + \tau_{RF}^2 + 32T\tau + 14\tau_{RF}\tau + 33\tau^2} \right) \quad (2.2)$$

This equation can also be further generalized to include additional periods, which we note resembles the method presented by Hennel et al. [82] with the added condition of encoding only non-zero spectral components. However, the finite truncation of the gradient waveform (more prominent for our abbreviated rendition) imposes a frequency limit based on the minimum permitted separation time τ_{RF} . In general this is not problematic for low frequencies when the period of the waveform is much larger than the separation time. However, when the period of the waveform approaches or exceeds the minimum separation time, the fidelity of the spectral components can become compromised as the gap between the gradients interrupts the periodicity. This can result in deviations from the target frequency in addition to significant spectral broadening. A useful empirical relationship for this limit proposed here is that this method is viable for frequencies that obey the relation $T > \tau_{RF}$ such that the period of the waveform is greater than the separation time between gradients. For a separation time of 7 ms – the minimum permitted on our system, this limit is found to be ~ 50 Hz.

2.2.2 Monte Carlo Optimization

The signal when kurtosis is introduced by a series expansion in b can be written as [26,27]:

$$S(b) = S_0 e^{-bD + \frac{b^2 D^2 K}{6}} e^{-\frac{TE}{T_2}} \quad (2.3)$$

where b is the b-value, D the apparent diffusion coefficient, K the kurtosis, T_2 the spin-spin relaxation time and TE the echo time. Monte Carlo simulations were used to optimize the SNR of the difference in kurtosis between PGSE and OGSE acquisitions

(ΔK) ; we define this quantity as:

$$\Delta K = K_{OGSE} - K_{PGSE} \quad (2.4)$$

The signal curve for both PGSE and OGSE acquisitions was generated using equation 2.3 at three different b-values of 0, a maximum b-value that was varied and a third intermediate b-value that was equal to half of the maximum. In order to maintain feasibility for clinical systems, the maximum frequency was limited to 45 Hz. Gaussian noise was added to the calculated PGSE and OGSE signals upon which the magnitude of the noisy signals were then fitted to equation 2.3 with a non-negative least squares algorithm to recover ADC and kurtosis values. These values were then used to calculate ΔK according to equation 2.4. This procedure was repeated for 2000 iterations per each frequency/b-value combination. Subsequently the SNR of ΔK was estimated as the mean of this set of values divided by the standard deviation. The b-values for OGSE and PGSE encoding were simulated for a gradient system with slew rate of 180 T/m/s and max gradient amplitude of 75 mT/m. To avoid the effects of higher order terms in the kurtosis signal expansion our simulations were limited to a maximum b-value of 2500 s/mm^2 . The TE was chosen to be the minimum allowable for each frequency; accordingly the TE dependence is implicitly reflected through the varied frequency.

Accurate simulation of the diffusion signal required *a priori* knowledge of the frequency dependence of the diffusivity $D(\omega)$ and kurtosis $K(\omega)$ to capture the time-dependence of both quantities. The model of the diffusion dispersion presented by Arbabi et al. [44] was used to infer $D(\omega)$ such that a unique diffusivity was assigned to each frequency. A similar relationship for $K(\omega)$ was also required, however no such characterization has yet been performed for the diffusion kurtosis. Rather, the multi-frequency measurements of mean kurtosis (MK) presented by Yang et al. [94] were fitted to a power law model. This model, reported as $K(\omega) = 0.93 - 0.0016\omega^{(0.78)}$ provided an

empirical relationship between frequency and MK enabling simulation of the frequency dependent kurtosis.

The entire simulation was repeated for alternate diffusion encoding schemes including nominal $N = 2$ cosine modulated OGSE (Figure 2.1B) and $N = 2.5$ OGSE to observe effects of adding additional periods. In addition to ΔK the SNR of ΔADC (defined similarly as $\Delta ADC = ADC_{OGSE} - ADC_{PGSE}$), was also evaluated in a manner identical to ΔK .

2.2.3 In Vivo Protocol

Five healthy participants (3 male, 2 female, mean age 26 ± 4 years) were scanned on a head-only 7 Tesla MRI scanner (Siemens Magnetom 7T Plus, Erlangen Germany). The scanner was equipped with a gradient system capable of a maximum gradient amplitude and slew rate of 80 mT/m and 333 T/m/s respectively, however to maintain clinical feasibility, the maximum gradient amplitude was limited to 75 mT/m and slew rate to 125 T/m/s. Approval for this study was granted by the Institutional Review Board at Western University, written informed consent was obtained from each participant prior to scanning.

The in vivo protocol consisted of an optimal (as determined from Section 2.2) and sub-optimal scan each conducted twice in a test and re-test fashion: subjects were scanned to acquire the test data and were subsequently removed from the scanner, repositioned and returned after a short period to obtain the re-test acquisitions. Diffusion weighted images (DWIs) were acquired with two diffusion weighting schemes each with three shells using b-values of 0, 1250 and 2500 s/mm^2 and 0, 1000, 2000 s/mm^2 constituting the optimal and sub-optimal scans respectively. Images were acquired at each shell using both PGSE ($f = 0$ Hz) and modified 23 Hz $N = 1.5$ OGSE encoding (see Figure 2.1A). PGSE and OGSE acquisitions were integrated into one scan such that all acquisitions required for ΔK map generation could be performed in a single scan.

Diffusion weighting for both scans was applied along 4-directions in a tetrahedral scheme to enable maximum achievable b-values [78]. The remaining acquisition details of both the optimal and sub-optimal scans were identical and were as follows: TE/TR = 91/6500 ms, FOV = 200 x 200 mm, matrix size = 100 x 100, 2174 Hz bandwidth, 38 slices, 2 mm^3 isotropic resolution, 8 averages. Images were acquired with 6/8 partial Fourier phase encoding using a single shot EPI readout. The acquisition time per scan was 14 minutes for a total scanning time of 56 minutes (2 x (2 x 14) minutes) not inclusive of the break between test/re-test sessions.

2.2.4 Image Analysis

Eddy current characterization was performed independently using a field-monitoring system (Skope MRT, Zurich Switzerland). Acquired k-space trajectories and field maps were utilized to correct for eddy current distortions through integration in an offline model-based image reconstruction algorithm. Principal component analysis based denoising [96] was also applied to the complex data during reconstruction. Following reconstruction, all diffusion-weighted images were processed with Gibbs ringing removal (MRtrix) upon which FSL’s BET tool [97] was used to perform brain extraction and mask generation. Re-test images were registered to test images by applying rigid affine transforms generated from $b = 0$ s/mm^2 images from each acquisition; registration was performed using ANTs software [98].

DWIs from each shell were directionally averaged and fitted on a voxel wise basis to the natural logarithm of equation 2.3 with a non-negative least squares algorithm to extract ADC and kurtosis parameters; we note the use a non-negative least squares fitting algorithm eliminates the potential for implausible negative kurtosis values. From the fitted data, mean ADC and apparent kurtosis maps were generated for the PGSE and OGSE acquisitions separately. We note the apparent kurtosis - as used here, is formally distinct from the mean kurtosis, the latter being derived from the diffusion

kurtosis tensor.

Dispersion maps of the ADC (ΔADC) and kurtosis (ΔK) were generated for each subject as the difference between PGSE and OGSE acquisitions; we define $\Delta K = K_{OGSE} - K_{PGSE}$ and $\Delta ADC = ADC_{OGSE} - ADC_{PGSE}$.

2.2.5 Re-test Analysis

ΔK maps generated from registered re-test DWIs were compared to test ΔK maps through a Bland-Altman analysis [99] for both the optimal ($b = 2500 \text{ s/mm}^2$) and sub-optimal ($b = 2000 \text{ s/mm}^2$) protocols. A minimum kurtosis threshold of 0.9 was applied to isolate white matter voxels upon which volumes from each subject were combined and were used to generate Bland-Altman plots of ΔK measurements. Coefficients of variation (CoVs) and standard deviations were calculated for both the optimal and sub-optimal scans to infer relative differences in SNR.

2.3 Results

2.3.1 Optimization Results

Optimization results in Figure 2.2 indicate the optimal frequency of 23 Hz was most influenced by differences in maximum b-value between frequencies. The optimal protocol to acquire ΔK maps was found to consist of 23 Hz OGSE with a b-value of 2500 s/mm^2 and a corresponding TE of 91 ms. The proposed $N = 1.5$ waveform (Figure 2.1A) achieves maximum SNR for both ΔK as well as ΔADC maps as seen in Figure 2.2B. We note the distinction in scaling in Figure 2.2B, with ΔADC maps having approximately 4 times higher SNR than ΔK .

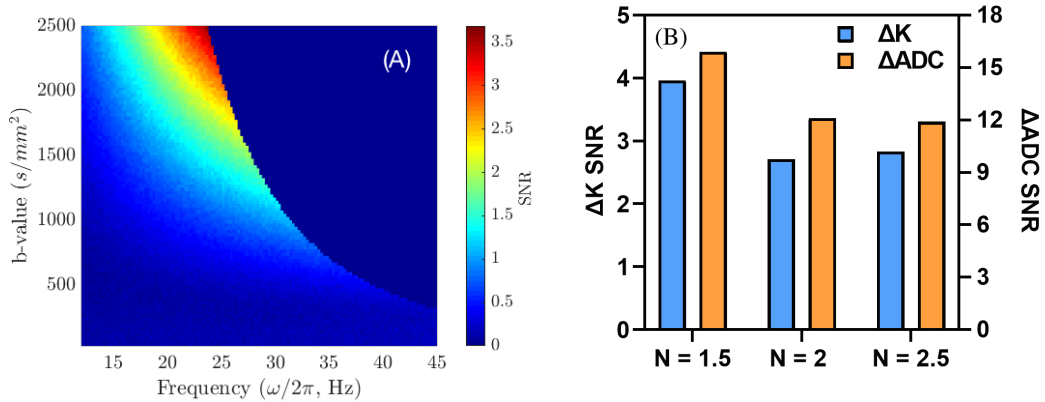


Figure 2.2: SNR of ΔK for varying b-value and frequency combinations (A) and comparisons of maximum possible SNR for $N = 1.5$, $N = 2$ and $N = 2.5$ oscillation periods for both ΔK and ΔADC maps (B).

2.3.2 in vivo Results

A trend of decreasing kurtosis and increasing ADC is observed when comparing OGSE to PGSE images (Figure 2.3). In frontal white matter ROIs (see Figure 2.3C) mean differences between OGSE and PGSE of approximately 10% and 14% are observed across subjects in apparent kurtosis and ADC values respectively. These differences constitute the contrast of the dispersion maps generated from PGSE and OGSE (Figure 2.4), showing comparable image quality across all subjects in both ΔK and ΔADC . Consistent measurements of ΔK were observed across participants in the genu, splenium and body of the corpus callosum (see Figure 2.5B) with no statistically significant differences observed between the regions. However, significantly larger absolute ΔK values ($p < 0.05$) were observed in the internal capsule of the corticospinal tract relative to the surrounding WM as seen in Figure 2.6.

The effect of applied diffusion weighting on ΔK maps is presented in Figure 2.7. A noticeable qualitative difference is observed when comparing the optimal and sub-optimal scans, with the lower b-value protocol exhibiting reduced SNR.

Bland-Altman plots comparing the test and re-test ΔK measurements across all volumes from each subject are shown in Figure 2.8. Mean Coefficients of variation (CoV)

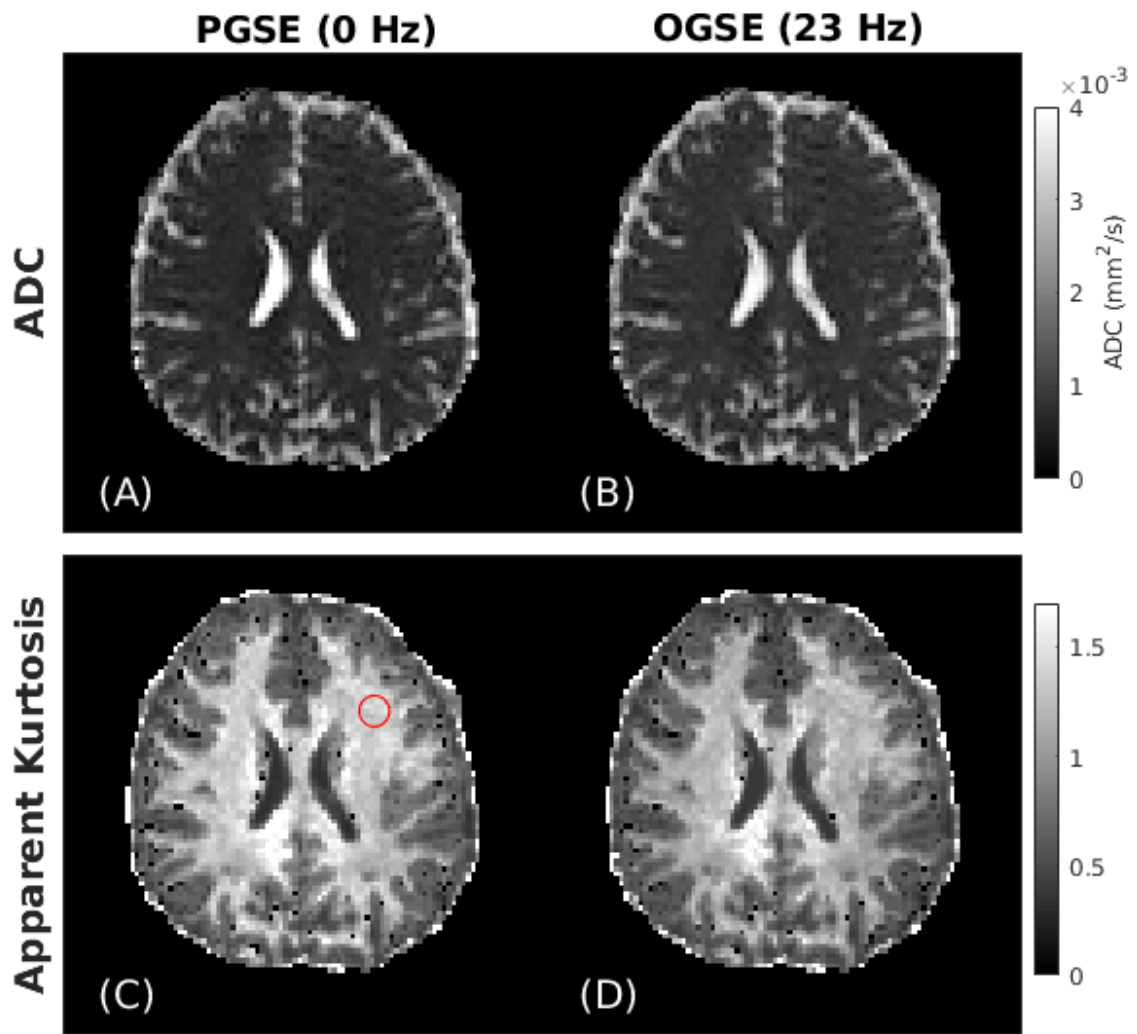


Figure 2.3: Generated ADC maps (top row) and apparent kurtosis maps (bottom row) from one healthy subject using both PGSE (A,C) and OGSE (B,D). An increase of ADC in parenchyma is observed in OGSE relative to PGSE in ADC maps and a reduction is demonstrated in apparent kurtosis maps. Also shown in (C) is an example ROI used for calculating mean differences between OGSE and PGSE.

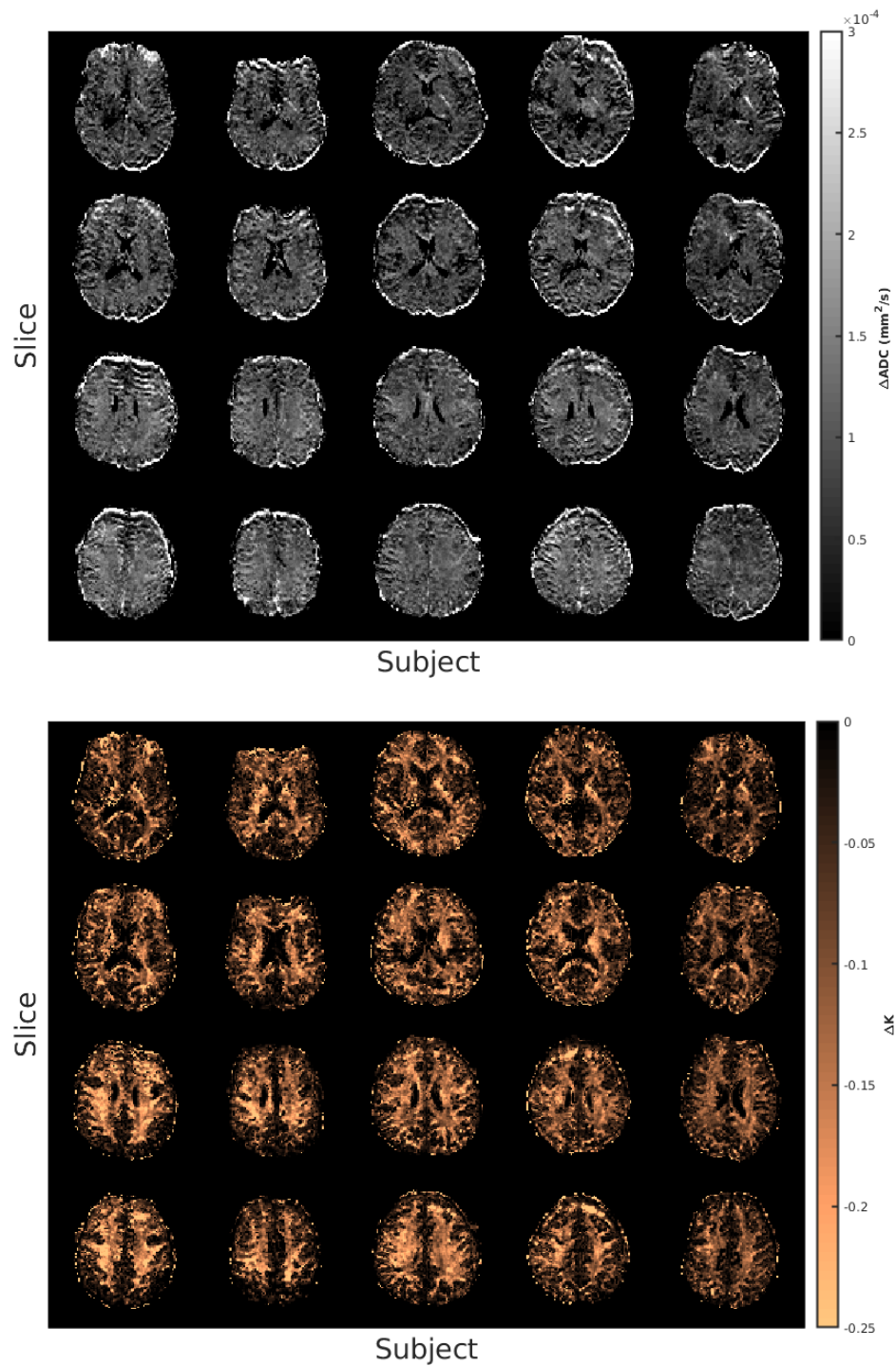


Figure 2.4: Generated ΔADC (top) and ΔK (bottom) maps for a few slices from each subject. Comparable image quality is observed across participants though some B_0 inhomogeneity induced distortions are apparent.

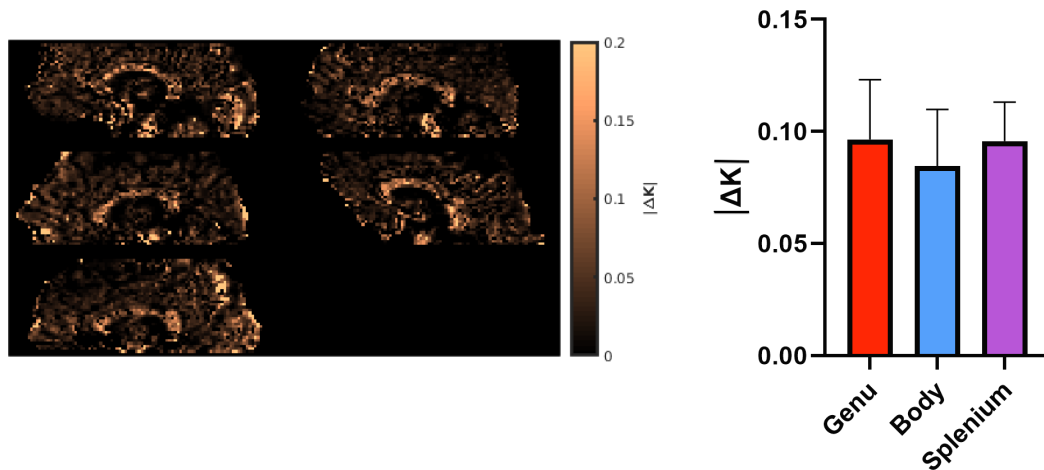


Figure 2.5: Sagittal slices of kurtosis dispersion maps showing the corpus callosum of each subject (left) and mean absolute ΔK values of different regions of the corpus callosum averaged across all subjects (right); error bars indicate the standard deviation. There is no statistically significant difference between regions.

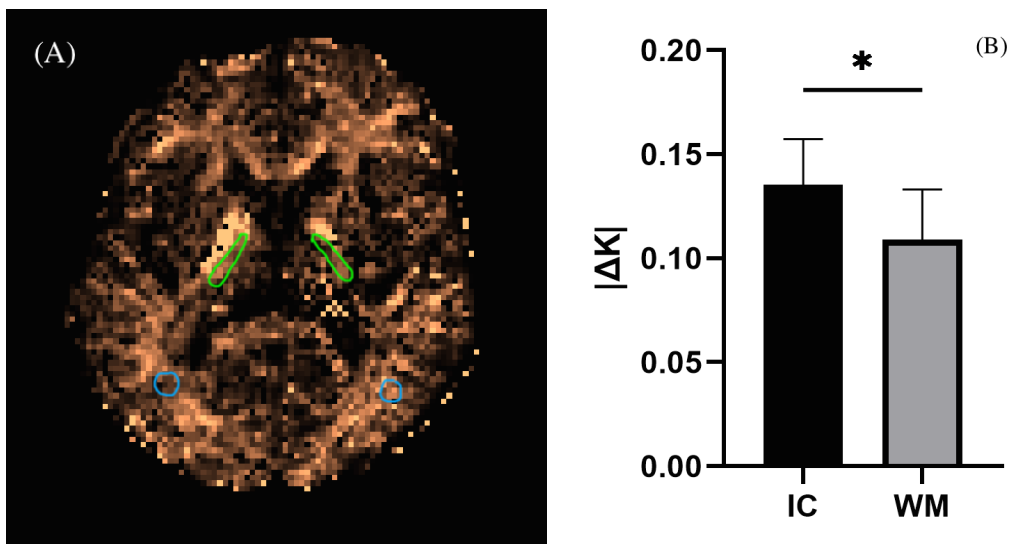


Figure 2.6: Example regions of interest (A) of the internal capsule (green) and posterior white matter (blue) regions. (B) comparison of mean absolute ΔK values across all subjects between the internal capsule (IC) and white matter (WM) ROIs, error bars denote the standard deviation. Here * denotes $p < 0.05$.

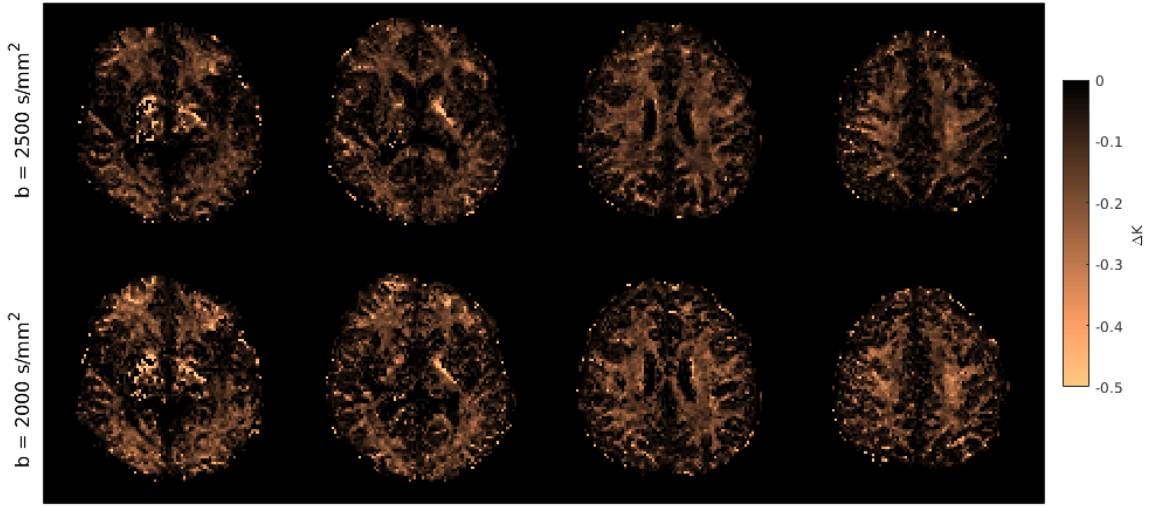
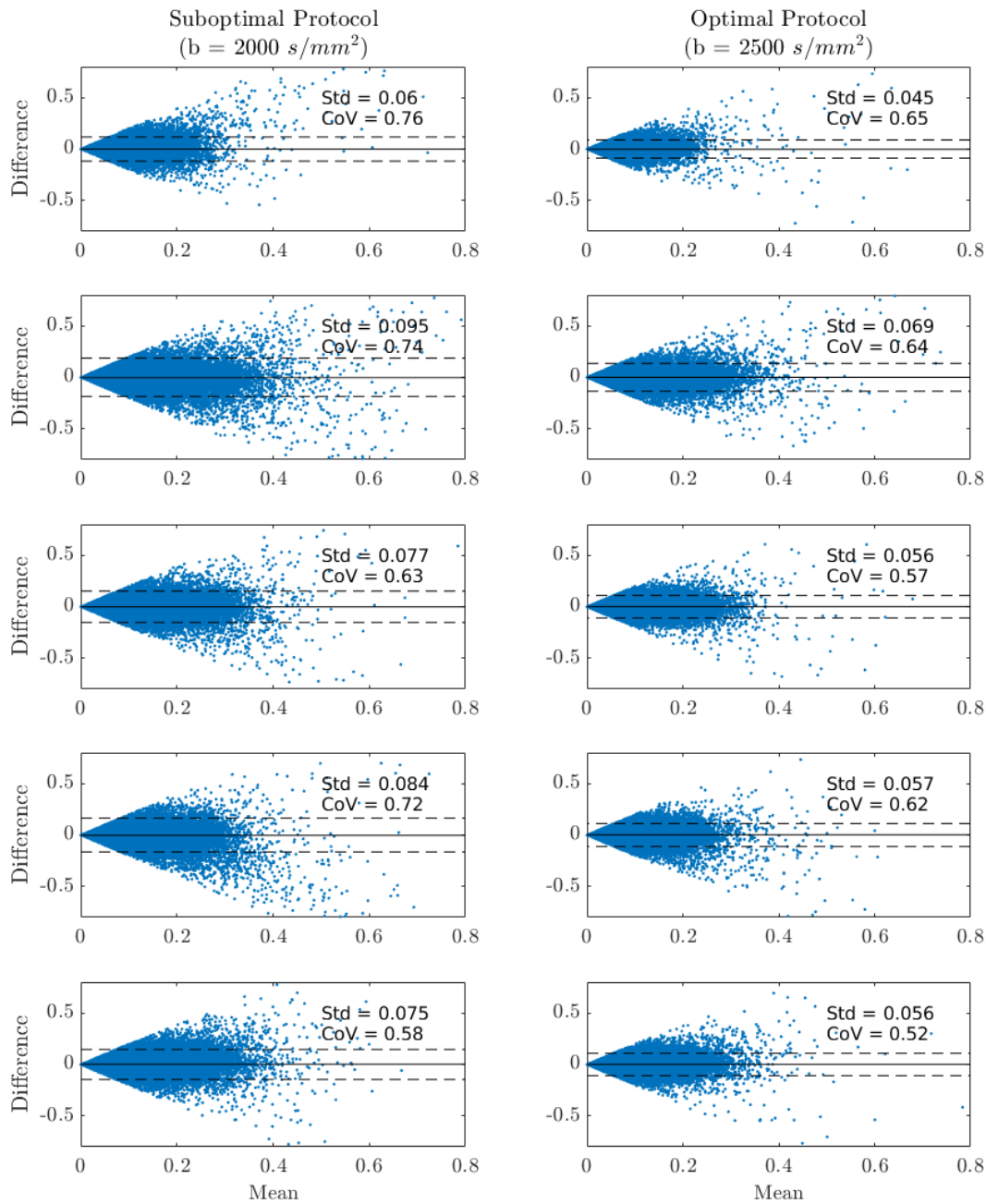


Figure 2.7: Comparison of optimal ($b = 2500 \text{ s/mm}^2$, top row) and suboptimal ($b = 2000 \text{ s/mm}^2$, bottom row) ΔK maps from one subject. A qualitative increase in noise is apparent in the suboptimal scans supporting the optimization results.

from ΔK maps across all subjects are reported as 0.60 and 0.69 for the optimal ($b = 2500 \text{ s/mm}^2$) and sub-optimal ($b = 2000 \text{ s/mm}^2$) scans respectively. The lower variation in the $b = 2500 \text{ s/mm}^2$ images suggests a higher SNR of ΔK which is also qualitatively observed in Figure 2.7 and consistent with the optimization results of Figure 2.2A. Moreover, mean CoVs for ΔADC maps were considerably lower and calculated to be 0.50 and 0.54 for the optimal and sub-optimal protocols respectively, demonstrating increased SNR relative to ΔK . This is supported by observations from Figure 2.2B that suggest an increased SNR for ΔADC maps when compared to ΔK . The trends observed in the coefficients of variation were mirrored in the standard deviations, which are also shown on the Bland-Altman plots in Figure 2.8.



Subjects

Figure 2.8: Bland Altman plots comparing test and re-test acquisitions for the $b = 2000$ (left column) and $b = 2500 \text{ s/mm}^2$ scans (right column) across all volumes from each subject; rows correspond to different subjects, columns correspond to the sub-optimal and optimal protocols. Also shown are the coefficients of variation (CoV) and standard deviations (Std). The dashed lines on each plot denote ± 1.96 standard deviations and the solid black line denotes the mean difference between the test and retest measurements.

2.4 Discussion

2.4.1 Waveform Remarks

This chapter demonstrates the first measurements of kurtosis in the human brain using oscillating gradients with a clinically relevant gradient system. The work was facilitated by the introduction of a bipolar OGSE gradient waveform that significantly reduces the TE of the acquisition. By effectively reducing the minimum number of periods to 1.5, significant gains in SNR were made possible through reduced TE. Optimization results confirm this configuration to be optimal for measurements of ΔK and ΔADC providing higher SNR for both when compared to OGSE performed with additional periods (see figure 2.2B). This result agrees with results from Arbabi et al. [44] that suggested a waveform with less than 2 periods would provide higher SNR than conventional $N \geq 2$ OGSE for ΔADC maps.

Despite these advantages, the shorter duration of the waveform further limits the range of possible b-values and as such our method is likely best suited for lower oscillation frequencies ($f < 40$ Hz) where the reduction in b-value due to oscillation is negated by the longer period of the waveform. This effect further justifies the use of the tetrahedral direction scheme, which critically enables the maximum gradient amplitude to be exploited in each direction simultaneously thereby maximizing the applied diffusion weighting [78]. While the tetrahedral scheme also prevents the use of DKI derived metrics associated with the diffusion kurtosis tensor and may introduce rotation variance [100], the directionally averaged kurtosis has been shown to be a useful and accurate reflection of MK derived from tensor fitting [35].

In addition, the method presented here inherently includes first-moment nulling to eliminate any spectral component at 0 Hz. While this change also provides flow-compensation to avoid perfusion effects, it may also be vital when performing ΔK or ΔADC map generation using PGSE and OGSE acquisitions. Spectral overlap between the two acquisitions

may result in signal loss when a difference is taken and hence eliminating overlapping components mitigates this potential issue.

2.4.2 In Vivo Findings

The ΔK maps demonstrate consistent differences between white (WM) and gray matter (GM) regions across all subjects as seen in Figure 2.4B. The larger negative ΔK in WM suggests that, somewhat surprisingly, 23 Hz is a sufficiently high frequency to be in a regime where diffusion becomes increasingly Gaussian and kurtosis begins to vanish, similar to findings at short diffusion times in the ex vivo spinal cord and mouse brain [65, 66]. This interpretation is supported by the pronounced negative ΔK observed in the internal capsule (see Figure 2.6) where the largest axons in the human brain are more prevalent [101, 102] and would thus trend towards Gaussian diffusion at lower frequencies than smaller axons. Expectedly however, our frequency is not high enough to observe significant changes between regions of the corpus callosum where differences in axon size are more subtle. While the proximity to the ventricles may make measurements in the corpus callosum more susceptible to cerebrospinal fluid partial volume effects [77], given the high diffusion weighting cerebrospinal fluid is not anticipated to contribute to these results. Moreover, lack of trends in the ΔK of the corpus callosum suggests higher frequencies may be required to observe finer structural changes even in dominant WM tracts [103]. Conversely, at even lower frequencies (i.e., longer diffusion times), it is expected that the trend of kurtosis with frequency will reverse due to the effects of permeability, contributing to observed non-monotonic behavior [65–68]. Notably, this transition frequency may be larger here compared to previous ex vivo samples due to axon shrinkage that is known to occur with sample fixation. Given that the diffusion times accessible through OGSE are shorter than typical exchange times derived from the Kärger model, our measurements lie in the short diffusion time regime where exchange and permeability effects that act to reduce the apparent kurtosis likely do not have a

significant role in these results [69,70]. Moreover, for this reason a monotonic model is likely appropriate to describe $K(\omega)$ in the context of OGSE measurements.

As observed in Figure 2.7 even relatively small decreases in b-value (20%) for the same frequency have noticeable impact on the SNR of produced ΔK maps. This effect is consistent with previous studies focusing on the optimization of kurtosis measurements [30, 33] and suggests the optimal ΔK protocol will favor increasingly larger diffusion weighting. Accordingly, future protocol designs should be attentive to the validity of equation 2.3 for $b \geq 3000 \text{ s/mm}^2$ beyond which higher order effects begin to emerge. Such limitations may be avoided by recalling the relation proposed by Jensen et al. [27], indicating that equation 2.3 remains valid so long as the condition $b < \frac{3}{KD}$ is satisfied. These effects were assumed to be conservatively avoided in this study by limiting the b-value of the acquisitions to 2500 s/mm^2 . However, the general increase in ΔK values for the sub-optimal (lower b-value) acquisition observed in Figure 2.7 may suggest some higher order effects are still present in our optimized protocol due to the increased b-value.

2.4.3 Applications

Observations of the frequency/time dependence of the kurtosis may constitute a novel biomarker, enabling further insight into physiological conditions influencing the degrees of diffusion restriction - similar to the utility of ΔADC [44,73,75,76]. Aggarwal et al. [65] observed significantly reduced ΔMK in regions of local demyelination due to increased permeability while Wu et al. [93] noted increases in ΔMK corresponding to regions of severe edema in a mouse model of hypoxic ischemic injury demonstrating the sensitivity of the frequency dependent kurtosis to various pathologies. Wu et al. [93] also noted significantly larger differences in kurtosis relative to differences in ADC between PGSE and OGSE, suggesting ΔK may be an equally prominent indicator of pathology.

Since our method does not require rapid slewing or extremely large gradient amplitudes our protocol can be easily adapted to full body scanners without exceeding

the specifications of modern conventional gradient systems. However despite this, the method presented here is still likely ill-suited to fully characterize the relationship between kurtosis and frequency, $K(\omega)$. The range of frequencies remains limited by the b-values required for observing kurtosis effects while the tetrahedral scheme prohibits the calculation of the diffusion kurtosis tensor. Consequently, a multi-frequency investigation would benefit from the performance presented by recent advancements in gradient coils [80,95]. As a result, our optimized protocol does not aim to replace high-performance gradient measurements but rather to compliment them, providing an efficient method to make frequency dependent kurtosis measurements more accessible on a wider variety of systems.

The primary limitation of this study however, remains the low SNR of the generated ΔK maps. The results of Figure 2.8 demonstrate large CoVs for both the optimal and sub-optimal protocols. Moreover, while our study avoids the use of high-performance gradients, it does benefit from the additional SNR that arises due to imaging at ultra-high field (7T). Equivalent measurements conducted at 3T would require approximately twice as many averages thereby further elongating the scan time. However, our technique will benefit from recent and on-going advancements in the field including non-Cartesian readouts such as single-shot spirals to provide increased SNR [104] or 3D multi-slab acquisitions [105]. Future work may also include the in-depth anatomical characterization of ΔK in addition to multi-frequency investigations of the time dependent kurtosis in the short diffusion-time regime that is made possible through oscillating gradients.

2.5 Conclusion

In this work we present a method for the generation of differential kurtosis maps on the basis of the kurtosis dispersion probed using oscillating gradients. Our optimized bipolar gradient waveform demonstrates maximum SNR for ΔK maps while also providing

considerably higher SNR for ΔADC maps compared to alternative OGSE encodings. Our results demonstrate these measurements are plausible on clinically relevant gradient systems and no longer restricted to high-performance gradient inserts. Moreover, our protocol constitutes a viable method for exploring the increasingly compelling evidence from rodent studies suggesting the role of the frequency dependent kurtosis as a multi-purpose biomarker.

Chapter 3

Conclusions

This chapter summarizes the themes presented in this thesis, it's context in the broader field and directions of future study.

3.1 Overview and Objective

Diffusion MRI constitutes a powerful tool to explore the microstructure of the brain through the monitoring of diffusing water molecules. The diffusion time dictates the length scales that may be probed by diffusing protons and as a result is vital for obtaining information regarding the degree of restricted diffusion imposed by microstructure. Oscillating gradient spin-echo (OGSE) is a diffusion MRI technique that enables access to shorter diffusion times than it's traditional pulsed gradient spin-echo (PGSE) counterpart via periodic modulation of the diffusion gradients. Due to technical limitations imposed by the required gradient waveforms the range of protocol parameters for OGSE, in particular combinations of frequency, b-value and TE, are severely limited. As a result applications of oscillating gradients in humans have been relatively sparse. Previous studies have focused almost exclusively on observing differences in the ADC between PGSE and OGSE and have demonstrated frequency dependent ADC measurements though none have yet to investigate the diffusion kurtosis with OGSE. Conventionally, the diffusion

kurtosis is only observable at large diffusion weighting (i.e. b -values $> 1000 \text{ s/mm}^2$) and as such has traditionally been beyond the capabilities of OGSE implemented on modern clinical gradients systems. While high-performance gradient systems can increase gradient amplitudes to make OGSE kurtosis imaging feasible, the prevalence of such hardware is limited restricting accessibility to select research groups. As a result, this thesis has presented a novel method for implementing oscillating gradients for diffusion kurtosis measurements using a clinically relevant gradient system.

3.2 Findings and Limitations

This objective was made possible by the use of a novel bipolar gradient waveform that reduced the TE of the acquisitions while retaining access to the high b -values required to observe kurtosis. Our optimized protocol demonstrated consistent negative kurtosis dispersion realized by decreases in kurtosis across all healthy human subjects ($n = 5$) in OGSE images relative to PGSE. Generated kurtosis dispersion maps visualize the spatial change in kurtosis with frequency and were observed to be elevated in areas of the corticospinal tract but consistent across regions of the corpus callosum. This may suggest some sensitivity to axon size with the corticospinal tract exhibiting some of the largest axons in the brain. Moreover, the inability to distinguish between regions of the corpus callosum suggests higher frequencies may be required to observe differences between these regions based on the disparity of their axon diameters. While permeability can also impact diffusion kurtosis measurements by altering the degree of restriction making membranes more or less penetrable to diffusing water molecules, since we are in the short diffusion time regime of OGSE we anticipate negligible contributions of exchange to our measurements. Despite suffering from low SNR our optimized protocol is the first to demonstrate kurtosis dispersion maps providing a new, unexplored approach to investigating time-dependent diffusion. Moreover, while our optimized bipolar method

is useful for investigating kurtosis, it may also prove valuable in future OGSE studies by providing access to lower frequencies and/or shorter TEs.

3.3 Future Work

Presently, the utility of the kurtosis dispersion (ΔK) remains relatively unexplored. Promising findings from small animal studies suggests ΔK may constitute a novel biomarker in the study of neurodegenerative diseases and brain injury. Inherent sensitivity to permeability effects have demonstrated uses for monitoring myelin integrity in mice, suggesting applications to neurodegenerative disorders such as multiple sclerosis. The unique contrast of ΔK , stemming from changes to microstructural permeability, may enable more effective detection of localized demyelination - permitting accurate lesion assessment. Similarly, the kurtosis dispersion's demonstrated sensitivity to spatial dimensions may be useful for detecting swelling in brain tissue. As observed in mice, possible applications include the detection of edema caused by ischemia or axonal beading due to traumatic injury. Confirmation of these findings in human subjects remains to be explored and should be a focal point of future study. Additionally, as microstructural models improve the understanding of both short and long diffusion time dynamics and their relation to pathology, new presently undiscovered clinical uses may arise.

In order to fully realize these applications however, imminent future work should focus on improving the SNR of acquired kurtosis dispersion maps. One promising avenue on this front is the incorporation of non-Cartesian readouts such as spirals to replace EPI and provide increased SNR for both kurtosis measurements and generated kurtosis dispersion maps. In addition, the reduced TE associated with spiral acquisitions may provide further flexibility in protocol design permitting multi-frequency investigations to explore the role of the frequency dependent kurtosis in the context of anatomical microstructure.

Appendix A

A.1 Derivation of Equation 2.2

We define the bipolar gradient waveform of Figure 2.1A in a piece-wise fashion as:

$$g(t) = \begin{cases} \frac{Gt}{\tau} & 0 \leq t \leq \tau \\ G & \tau \leq t \leq \tau + L \\ \frac{GL}{\tau} - \frac{Gt}{\tau} + 2G & \tau + L \leq t \leq 3\tau + L \\ -G & 3\tau + L \leq t \leq 3\tau + L + T \\ \frac{Gt}{\tau} - \left(\frac{TG}{\tau} + \frac{GL}{\tau} + 4G \right) & 3\tau + L + T \leq t \leq 4\tau + L + T \\ 0 & 4\tau + L + T \leq t \leq 4\tau + L + T + \tau_{RF} \\ \frac{Gt}{\tau} - \frac{G(T+L+4\tau+\tau_{RF})}{\tau} & T + L + 4\tau + \tau_{RF} < t < T + L + 5\tau + \tau_{RF} \\ G & T + L + 5\tau + \tau_{RF} < t < 2T + L + 5\tau + \tau_{RF} \\ \frac{G(2T+L+6\tau+\tau_{RF})}{\tau} - \frac{Gt}{\tau} & 2T + L + 5\tau + \tau_{RF} < t < 2T + L + 7\tau + \tau_{RF} \\ -G & 2T + L + 7\tau + \tau_{RF} < t < T + 2L + 7\tau + \tau_{RF} \\ \frac{Gt}{\tau} - \frac{G(2T+2L+8\tau+\tau_{RF})}{\tau} & 2T + 2L + 7\tau + \tau_{RF} < t < 2T + 2L + 8\tau + \tau_{RF} \end{cases} \quad (\text{A.1})$$

where G is the maximum gradient amplitude, τ is the gradient rise time (also known as ramp time), L is the duration the initial positive lobe, T is the duration of the sec-

ond negative lobe and τ_{RF} is the separation time required for the refocusing RF pulse. Performing $\int g(t)dt$ in a piece-wise fashion yields an expression for the zeroth moment as:

$$\int_0^{2T+2L+8\tau+\tau_{RF}} g(t)dt = \frac{G(2T + 2L + 8\tau + \tau_{RF})^2}{2\tau} - \frac{G\left(2Lt - \frac{t^2}{2} + 2Tt + 8\tau t + t\tau_{RF}\right)}{\tau} \quad (\text{A.2})$$

integrating once more it is possible to obtain the integral of the zeroth moment:

$$G\left(-T\tau - T(T + \tau_{RF}) + L^2 + L(2T + 7\tau + \tau_{RF}) + 4\tau^2\right) - \frac{G(2T + 2L - t + 8\tau + \tau_{RF})^3}{6\tau} \quad (\text{A.3})$$

Setting the integral of the zeroth moment (Equation A.3) to zero and solving the equation for L allows the duration of the initial gradient to be determined (taking the positive root) as:

$$L = \frac{1}{2} \left(\sqrt{8T^2 + 32T\tau + 8T\tau_{RF} + 33\tau^2 + \tau_{RF}^2 + 14\tau\tau_{RF} - 2T - 7\tau - \tau_{RF}} \right) \quad (\text{A.4})$$

Bibliography

- [1] R. Brown, “Xxvii. a brief account of microscopical observations made in the months of june, july and august 1827, on the particles contained in the pollen of plants; and on the general existence of active molecules in organic and inorganic bodies,” *The philosophical magazine*, vol. 4, no. 21, pp. 161–173, 1828.
- [2] A. Einstein, *Investigations on the Theory of the Brownian Movement*. Dover Publications, 1956.
- [3] F. Waxman, *The axon: structure, function, and pathophysiology*. Oxford University Press, USA, 1995.
- [4] C. Beaulieu, “The basis of anisotropic water diffusion in the nervous system—a technical review,” *NMR in Biomedicine: An International Journal Devoted to the Development and Application of Magnetic Resonance In Vivo*, vol. 15, no. 7-8, pp. 435–455, 2002.
- [5] M. E. Moseley, J. Kucharczyk, H. S. Asgari, and D. Norman, “Anisotropy in diffusion-weighted mri,” *Magnetic Resonance in Medicine*, vol. 19, no. 2, pp. 321–326, 1991.
- [6] T. F. Weiss, *Cellular Biophysics: Volume 1: Transport*. MIT Press, 1995.
- [7] D. K. Jones, *Diffusion mri*. Oxford University Press, 2010.
- [8] D. Le Bihan, J.-F. Mangin, C. Poupon, C. A. Clark, S. Pappata, N. Molko, and H. Chabriat, “Diffusion tensor imaging: concepts and applications,” *Journal of Magnetic Resonance Imaging: An Official Journal of the International Society for Magnetic Resonance in Medicine*, vol. 13, no. 4, pp. 534–546, 2001.
- [9] M. A. Horsfield and D. K. Jones, “Applications of diffusion-weighted and diffusion tensor mri to white matter diseases—a review,” *NMR in Biomedicine: An International Journal Devoted to the Development and Application of Magnetic Resonance In Vivo*, vol. 15, no. 7-8, pp. 570–577, 2002.
- [10] D. M. Patterson, A. R. Padhani, and D. J. Collins, “Technology insight: water diffusion mri—a potential new biomarker of response to cancer therapy,” *Nature clinical practice Oncology*, vol. 5, no. 4, pp. 220–233, 2008.

- [11] H. C. Torrey, "Bloch equations with diffusion terms," *Physical review*, vol. 104, no. 3, p. 563, 1956.
- [12] E. O. Stejskal and J. E. Tanner, "Spin diffusion measurements: spin echoes in the presence of a time-dependent field gradient," *The journal of chemical physics*, vol. 42, no. 1, pp. 288–292, 1965.
- [13] J. E. Tanner and E. O. Stejskal, "Restricted self-diffusion of protons in colloidal systems by the pulsed-gradient, spin-echo method," *The Journal of Chemical Physics*, vol. 49, no. 4, pp. 1768–1777, 1968.
- [14] E. D. Finch, J. F. Harmon, and B. H. Muller, "Pulsed nmr measurements of the diffusion constant of water in muscle," *Archives of Biochemistry and Biophysics*, vol. 147, no. 1, pp. 299–310, 1971.
- [15] J. Andrasko, "Water diffusion permeability of human erythrocytes studied by a pulsed gradient nmr technique," *Biochimica et Biophysica Acta (BBA)-General Subjects*, vol. 428, no. 2, pp. 304–311, 1976.
- [16] V. Kenkre, E. Fukushima, and D. Sheltraw, "Simple solutions of the torrey–bloch equations in the nmr study of molecular diffusion," *Journal of Magnetic Resonance*, vol. 128, no. 1, pp. 62–69, 1997.
- [17] D. Le Bihan, E. Breton, D. Lallemand, P. Grenier, E. Cabanis, and M. Laval-Jeantet, "Mr imaging of intravoxel incoherent motions: application to diffusion and perfusion in neurologic disorders.," *Radiology*, vol. 161, no. 2, pp. 401–407, 1986.
- [18] D. Le Bihan and E. Breton, "Imagerie de diffusion in vivo par résonance magnétique nucléaire," *Comptes rendus de l'Académie des sciences. Série 2, Mécanique, Physique, Chimie, Sciences de l'univers, Sciences de la Terre*, vol. 301, no. 15, pp. 1109–1112, 1985.
- [19] P. J. Basser, J. Mattiello, and D. LeBihan, "Estimation of the effective self-diffusion tensor from the nmr spin echo," *Journal of Magnetic Resonance, Series B*, vol. 103, no. 3, pp. 247–254, 1994.
- [20] P. J. Basser, J. Mattiello, and D. LeBihan, "Mr diffusion tensor spectroscopy and imaging," *Biophysical journal*, vol. 66, no. 1, pp. 259–267, 1994.
- [21] P. J. Basser and C. Pierpaoli, "A simplified method to measure the diffusion tensor from seven mr images," *Magnetic resonance in medicine*, vol. 39, no. 6, pp. 928–934, 1998.
- [22] C. Lebel, T. Benner, and C. Beaulieu, "Six is enough? comparison of diffusion parameters measured using six or more diffusion-encoding gradient directions with deterministic tractography," *Magnetic resonance in medicine*, vol. 68, no. 2, pp. 474–483, 2012.

- [23] A. H. Poonawalla and X. J. Zhou, “Analytical error propagation in diffusion anisotropy calculations,” *Journal of Magnetic Resonance Imaging: An Official Journal of the International Society for Magnetic Resonance in Medicine*, vol. 19, no. 4, pp. 489–498, 2004.
- [24] Q. Dong, R. C. Welsh, T. L. Chenevert, R. C. Carlos, P. Maly-Sundgren, D. M. Gomez-Hassan, and S. K. Mukherji, “Clinical applications of diffusion tensor imaging,” *Journal of Magnetic Resonance Imaging: An Official Journal of the International Society for Magnetic Resonance in Medicine*, vol. 19, no. 1, pp. 6–18, 2004.
- [25] P. Sundgren, Q. Dong, D. Gomez-Hassan, S. Mukherji, P. Maly, and R. Welsh, “Diffusion tensor imaging of the brain: review of clinical applications,” *Neuroradiology*, vol. 46, no. 5, pp. 339–350, 2004.
- [26] J. H. Jensen, J. A. Helpert, A. Ramani, H. Lu, and K. Kaczynski, “Diffusional kurtosis imaging: the quantification of non-gaussian water diffusion by means of magnetic resonance imaging,” *Magnetic Resonance in Medicine: An Official Journal of the International Society for Magnetic Resonance in Medicine*, vol. 53, no. 6, pp. 1432–1440, 2005.
- [27] J. H. Jensen and J. A. Helpert, “Mri quantification of non-gaussian water diffusion by kurtosis analysis,” *NMR in Biomedicine*, vol. 23, no. 7, pp. 698–710, 2010.
- [28] A. J. Steven, J. Zhuo, and E. R. Melhem, “Diffusion kurtosis imaging: an emerging technique for evaluating the microstructural environment of the brain,” *American journal of roentgenology*, vol. 202, no. 1, pp. W26–W33, 2014.
- [29] A. B. Rosenkrantz, A. R. Padhani, T. L. Chenevert, D.-M. Koh, F. De Keyser, B. Taouli, and D. Le Bihan, “Body diffusion kurtosis imaging: basic principles, applications, and considerations for clinical practice,” *Journal of Magnetic Resonance Imaging*, vol. 42, no. 5, pp. 1190–1202, 2015.
- [30] D. H. Poot, J. Arnold, E. Achten, M. Verhoye, and J. Sijbers, “Optimal experimental design for diffusion kurtosis imaging,” *IEEE transactions on medical imaging*, vol. 29, no. 3, pp. 819–829, 2010.
- [31] A. Chuhutin, B. Hansen, and S. N. Jespersen, “Precision and accuracy of diffusion kurtosis estimation and the influence of b-value selection,” *NMR in Biomedicine*, vol. 30, no. 11, p. e3777, 2017.
- [32] B. Hansen and S. N. Jespersen, “Data for evaluation of fast kurtosis strategies, b-value optimization and exploration of diffusion mri contrast,” *Scientific data*, vol. 3, no. 1, pp. 1–5, 2016.
- [33] N. Gilani, P. N. Malcolm, and G. Johnson, “Parameter estimation error dependency on the acquisition protocol in diffusion kurtosis imaging,” *Applied magnetic resonance*, vol. 47, no. 11, pp. 1229–1238, 2016.

- [34] X. Yan, M. Zhou, L. Ying, D. Yin, M. Fan, G. Yang, Y. Zhou, F. Song, and D. Xu, "Evaluation of optimized b-value sampling schemas for diffusion kurtosis imaging with an application to stroke patient data," *Computerized medical imaging and graphics*, vol. 37, no. 4, pp. 272–280, 2013.
- [35] R. N. Henriques, S. N. Jespersen, D. K. Jones, and J. Veraart, "Toward more robust and reproducible diffusion kurtosis imaging," *Magnetic Resonance in Medicine*, 2021.
- [36] B. Gross and R. Kosfeld, "Anwendung der spin-echo-methode der messung der selbstdiffusion," *Messtechnik*, vol. 77, pp. 171–177, 1969.
- [37] J. Stepišnik, "Analysis of nmr self-diffusion measurements by a density matrix calculation," *Physica B+ C*, vol. 104, no. 3, pp. 350–364, 1981.
- [38] P. T. Callaghan and J. Stepišnik, "Frequency-domain analysis of spin motion using modulated-gradient nmr," 1995.
- [39] A. T. Van, S. J. Holdsworth, and R. Bammer, "In vivo investigation of restricted diffusion in the human brain with optimized oscillating diffusion gradient encoding," *Magnetic resonance in medicine*, vol. 71, no. 1, pp. 83–94, 2014.
- [40] J. Xu, "Probing neural tissues at small scales: Recent progress of oscillating gradient spin echo (ogse) neuroimaging in humans," *Journal of neuroscience methods*, p. 109024, 2020.
- [41] M. D. Does, E. C. Parsons, and J. C. Gore, "Oscillating gradient measurements of water diffusion in normal and globally ischemic rat brain," *Magnetic Resonance in Medicine: An Official Journal of the International Society for Magnetic Resonance in Medicine*, vol. 49, no. 2, pp. 206–215, 2003.
- [42] C. A. Baron and C. Beaulieu, "Oscillating gradient spin-echo (ogse) diffusion tensor imaging of the human brain," *Magnetic resonance in medicine*, vol. 72, no. 3, pp. 726–736, 2014.
- [43] D. S. Novikov, E. Fieremans, S. N. Jespersen, and V. G. Kiselev, "Quantifying brain microstructure with diffusion mri: Theory and parameter estimation," *NMR in Biomedicine*, vol. 32, no. 4, p. e3998, 2019.
- [44] A. Arbabi, J. Kai, A. R. Khan, and C. A. Baron, "Diffusion dispersion imaging: Mapping oscillating gradient spin-echo frequency dependence in the human brain," *Magnetic resonance in medicine*, vol. 83, no. 6, pp. 2197–2208, 2020.
- [45] D. Wu, L. J. Martin, F. J. Northington, and J. Zhang, "Oscillating gradient diffusion mri reveals unique microstructural information in normal and hypoxia-ischemia injured mouse brains," *Magnetic resonance in medicine*, vol. 72, no. 5, pp. 1366–1374, 2014.

- [46] M. Aggarwal, M. V. Jones, P. A. Calabresi, S. Mori, and J. Zhang, “Probing mouse brain microstructure using oscillating gradient diffusion mri,” *Magnetic resonance in medicine*, vol. 67, no. 1, pp. 98–109, 2012.
- [47] D. C. Colvin, T. E. Yankeelov, M. D. Does, Z. Yue, C. Quarles, and J. C. Gore, “New insights into tumor microstructure using temporal diffusion spectroscopy,” *Cancer research*, vol. 68, no. 14, pp. 5941–5947, 2008.
- [48] D. C. Colvin, M. E. Loveless, M. D. Does, Z. Yue, T. E. Yankeelov, and J. C. Gore, “Earlier detection of tumor treatment response using magnetic resonance diffusion imaging with oscillating gradients,” *Magnetic resonance imaging*, vol. 29, no. 3, pp. 315–323, 2011.
- [49] D. Wu, L. J. Martin, F. J. Northington, and J. Zhang, “Oscillating-gradient diffusion magnetic resonance imaging detects acute subcellular structural changes in the mouse forebrain after neonatal hypoxia-ischemia,” *Journal of Cerebral Blood Flow & Metabolism*, vol. 39, no. 7, pp. 1336–1348, 2019.
- [50] M. Aggarwal, J. Burnsed, L. J. Martin, F. J. Northington, and J. Zhang, “Imaging neurodegeneration in the mouse hippocampus after neonatal hypoxia–ischemia using oscillating gradient diffusion mri,” *Magnetic resonance in medicine*, vol. 72, no. 3, pp. 829–840, 2014.
- [51] O. Reynaud, K. V. Winters, D. M. Hoang, Y. Z. Wadghiri, D. S. Novikov, and S. G. Kim, “Surface-to-volume ratio mapping of tumor microstructure using oscillating gradient diffusion weighted imaging,” *Magnetic resonance in medicine*, vol. 76, no. 1, pp. 237–247, 2016.
- [52] O. Reynaud, K. V. Winters, D. M. Hoang, Y. Z. Wadghiri, D. S. Novikov, and S. G. Kim, “Pulsed and oscillating gradient mri for assessment of cell size and extracellular space (pomace) in mouse gliomas,” *NMR in biomedicine*, vol. 29, no. 10, pp. 1350–1363, 2016.
- [53] X. Jiang, H. Li, J. Xie, P. Zhao, J. C. Gore, and J. Xu, “Quantification of cell size using temporal diffusion spectroscopy,” *Magnetic resonance in medicine*, vol. 75, no. 3, pp. 1076–1085, 2016.
- [54] I. Drobnjak, H. Zhang, A. Ianuș, E. Kaden, and D. C. Alexander, “Pgse, ogse, and sensitivity to axon diameter in diffusion mri: insight from a simulation study,” *Magnetic resonance in medicine*, vol. 75, no. 2, pp. 688–700, 2016.
- [55] K. D. Harkins, C. Beaulieu, J. Xu, J. C. Gore, and M. D. Does, “A simple estimate of axon size with diffusion mri,” *NeuroImage*, vol. 227, p. 117619, 2021.
- [56] J. Xu, H. Li, K. Li, K. D. Harkins, X. Jiang, J. Xie, H. Kang, R. D. Dortch, A. W. Anderson, M. D. Does, *et al.*, “Fast and simplified mapping of mean axon diameter using temporal diffusion spectroscopy,” *NMR in Biomedicine*, vol. 29, no. 4, pp. 400–410, 2016.

- [57] E. C. Parsons Jr, M. D. Does, and J. C. Gore, “Temporal diffusion spectroscopy: theory and implementation in restricted systems using oscillating gradients,” *Magnetic Resonance in Medicine: An Official Journal of the International Society for Magnetic Resonance in Medicine*, vol. 55, no. 1, pp. 75–84, 2006.
- [58] J. C. Gore, J. Xu, D. C. Colvin, T. E. Yankeelov, E. C. Parsons, and M. D. Does, “Characterization of tissue structure at varying length scales using temporal diffusion spectroscopy,” *NMR in Biomedicine*, vol. 23, no. 7, pp. 745–756, 2010.
- [59] J. Xu, M. D. Does, and J. C. Gore, “Quantitative characterization of tissue microstructure with temporal diffusion spectroscopy,” *Journal of magnetic resonance*, vol. 200, no. 2, pp. 189–197, 2009.
- [60] H. Li, J. C. Gore, and J. Xu, “Fast and robust measurement of microstructural dimensions using temporal diffusion spectroscopy,” *Journal of magnetic resonance*, vol. 242, pp. 4–9, 2014.
- [61] X. Jiang, H. Li, J. Xie, E. T. McKinley, P. Zhao, J. C. Gore, and J. Xu, “In vivo imaging of cancer cell size and cellularity using temporal diffusion spectroscopy,” *Magnetic resonance in medicine*, vol. 78, no. 1, pp. 156–164, 2017.
- [62] J. Xu, K. Li, R. A. Smith, J. C. Waterton, P. Zhao, H. Chen, M. D. Does, H. C. Manning, and J. C. Gore, “Characterizing tumor response to chemotherapy at various length scales using temporal diffusion spectroscopy,” *PloS one*, vol. 7, no. 7, p. e41714, 2012.
- [63] J. Xu, X. Jiang, H. Li, L. R. Arlinghaus, E. T. McKinley, S. P. Devan, B. M. Hardy, J. Xie, H. Kang, A. B. Chakravarthy, *et al.*, “Magnetic resonance imaging of mean cell size in human breast tumors,” *Magnetic resonance in medicine*, vol. 83, no. 6, pp. 2002–2014, 2020.
- [64] J. Xu, X. Jiang, S. P. Devan, L. R. Arlinghaus, E. T. McKinley, J. Xie, Z. Zu, Q. Wang, A. B. Chakravarthy, Y. Wang, *et al.*, “Mri-cytometry: Mapping nonparametric cell size distributions using diffusion mri,” *Magnetic resonance in medicine*, vol. 85, no. 2, pp. 748–761, 2021.
- [65] M. Aggarwal, M. D. Smith, and P. A. Calabresi, “Diffusion-time dependence of diffusional kurtosis in the mouse brain,” *Magnetic resonance in medicine*, vol. 84, no. 3, pp. 1564–1578, 2020.
- [66] S. N. Jespersen, J. L. Olesen, B. Hansen, and N. Shemesh, “Diffusion time dependence of microstructural parameters in fixed spinal cord,” *Neuroimage*, vol. 182, pp. 329–342, 2018.
- [67] S. Portnoy, J. Flint, S. Blackband, and G. Stanisz, “Oscillating and pulsed gradient diffusion magnetic resonance microscopy over an extended b-value range: implications for the characterization of tissue microstructure,” *Magnetic resonance in medicine*, vol. 69, no. 4, pp. 1131–1145, 2013.

- [68] N. Pyatigorskaya, D. Le Bihan, O. Reynaud, and L. Ciobanu, “Relationship between the diffusion time and the diffusion mri signal observed at 17.2 tesla in the healthy rat brain cortex,” *Magnetic resonance in medicine*, vol. 72, no. 2, pp. 492–500, 2014.
- [69] M. Nilsson, D. van Westen, F. Ståhlberg, P. C. Sundgren, and J. Lätt, “The role of tissue microstructure and water exchange in biophysical modelling of diffusion in white matter,” *Magnetic Resonance Materials in Physics, Biology and Medicine*, vol. 26, no. 4, pp. 345–370, 2013.
- [70] H.-H. Lee, A. Papaioannou, D. S. Novikov, and E. Fieremans, “In vivo observation and biophysical interpretation of time-dependent diffusion in human cortical gray matter,” *NeuroImage*, vol. 222, p. 117054, 2020.
- [71] C. A. Baron, M. Kate, L. Gioia, K. Butcher, D. Emery, M. Budde, and C. Beaulieu, “Reduction of diffusion-weighted imaging contrast of acute ischemic stroke at short diffusion times,” *Stroke*, vol. 46, no. 8, pp. 2136–2141, 2015.
- [72] A. Boonrod, A. Hagiwara, M. Hori, I. Fukunaga, C. Andica, T. Maekawa, and S. Aoki, “Reduced visualization of cerebral infarction on diffusion-weighted images with short diffusion times,” *Neuroradiology*, vol. 60, no. 9, pp. 979–982, 2018.
- [73] M. Iima, A. Yamamoto, M. Kataoka, Y. Yamada, K. Omori, T. Feiweier, and K. Togashi, “Time-dependent diffusion mri to distinguish malignant from benign head and neck tumors,” *Journal of Magnetic Resonance Imaging*, vol. 50, no. 1, pp. 88–95, 2019.
- [74] D. S. Novikov, J. H. Jensen, J. A. Helpert, and E. Fieremans, “Revealing mesoscopic structural universality with diffusion,” *Proceedings of the National Academy of Sciences*, vol. 111, no. 14, pp. 5088–5093, 2014.
- [75] F. Gao, X. Shen, H. Zhang, R. Ba, X. Ma, C. Lai, J. Zhang, Y. Zhang, and D. Wu, “Feasibility of oscillating and pulsed gradient diffusion mri to assess neonatal hypoxia-ischemia on clinical systems,” *Journal of Cerebral Blood Flow & Metabolism*, p. 0271678X20944353, 2020.
- [76] D. Wu, Y. Zhang, B. Cheng, S. Mori, R. H. Reeves, and F. J. Gao, “Time-dependent diffusion mri probes cerebellar microstructural alterations in a mouse model of down syndrome,” *Brain communications*, vol. 3, no. 2, p. fcab062, 2021.
- [77] P. Tétreault, K. D. Harkins, C. A. Baron, R. Stobbe, M. D. Does, and C. Beaulieu, “Diffusion time dependency along the human corpus callosum and exploration of age and sex differences as assessed by oscillating gradient spin-echo diffusion tensor imaging,” *NeuroImage*, vol. 210, p. 116533, 2020.
- [78] T. E. Conturo, R. C. McKinstry, E. Akbudak, and B. H. Robinson, “Encoding of anisotropic diffusion with tetrahedral gradients: a general mathematical diffusion formalism and experimental results,” *Magnetic Resonance in Medicine*, vol. 35, no. 3, pp. 399–412, 1996.

- [79] J. A. McNab, B. L. Edlow, T. Witzel, S. Y. Huang, H. Bhat, K. Heberlein, T. Feiweier, K. Liu, B. Keil, J. Cohen-Adad, *et al.*, “The human connectome project and beyond: initial applications of 300 mt/m gradients,” *Neuroimage*, vol. 80, pp. 234–245, 2013.
- [80] T. K. Foo, E. T. Tan, M. E. Vermilyea, Y. Hua, E. W. Fiveland, J. E. Piel, K. Park, J. Ricci, P. S. Thompson, D. Graziani, *et al.*, “Highly efficient head-only magnetic field insert gradient coil for achieving simultaneous high gradient amplitude and slew rate at 3.0 t (magnus) for brain microstructure imaging,” *Magnetic resonance in medicine*, vol. 83, no. 6, pp. 2356–2369, 2020.
- [81] K. Setsompop, R. Kimmilingen, E. Eberlein, T. Witzel, J. Cohen-Adad, J. A. McNab, B. Keil, M. D. Tisdall, P. Hoecht, P. Dietz, *et al.*, “Pushing the limits of in vivo diffusion mri for the human connectome project,” *Neuroimage*, vol. 80, pp. 220–233, 2013.
- [82] F. Hennel, E. S. Michael, and K. P. Pruessmann, “Improved gradient waveforms for oscillating gradient spin-echo (ogse) diffusion tensor imaging,” *NMR in Biomedicine*, vol. 34, no. 2, p. e4434, 2021.
- [83] E. T. Tan, R. Y. Shih, J. Mitra, T. Sprenger, Y. Hua, C. Bhushan, M. A. Bernstein, J. A. McNab, J. K. DeMarco, V. B. Ho, *et al.*, “Oscillating diffusion-encoding with a high gradient-amplitude and high slew-rate head-only gradient for human brain imaging,” *Magnetic resonance in medicine*, vol. 84, no. 2, pp. 950–965, 2020.
- [84] C. Ahn and Z. Cho, “Analysis of the eddy-current induced artifacts and the temporal compensation in nuclear magnetic resonance imaging,” *IEEE transactions on medical imaging*, vol. 10, no. 1, pp. 47–52, 1991.
- [85] J. Van Vaals and A. Bergman, “Optimization of eddy-current compensation,” *Journal of Magnetic Resonance (1969)*, vol. 90, no. 1, pp. 52–70, 1990.
- [86] N. Bodammer, J. Kaufmann, M. Kanowski, and C. Tempelmann, “Eddy current correction in diffusion-weighted imaging using pairs of images acquired with opposite diffusion gradient polarity,” *Magnetic Resonance in Medicine: An Official Journal of the International Society for Magnetic Resonance in Medicine*, vol. 51, no. 1, pp. 188–193, 2004.
- [87] J. J. Valsamis, P. I. Dubovan, and C. A. Baron, “Characterization and correction of time-varying eddy currents for diffusion mri,” *arXiv preprint arXiv:2102.00525*, 2021.
- [88] J. Zhang, G. Lemberskiy, L. Moy, E. Fieremans, D. S. Novikov, and S. G. Kim, “Measurement of cellular-interstitial water exchange time in tumors based on diffusion-time-dependent diffusional kurtosis imaging,” *NMR in Biomedicine*, vol. 34, no. 6, p. e4496, 2021.

- [89] J. Xu, H. Li, K. D. Harkins, X. Jiang, J. Xie, H. Kang, M. D. Does, and J. C. Gore, “Mapping mean axon diameter and axonal volume fraction by mri using temporal diffusion spectroscopy,” *Neuroimage*, vol. 103, pp. 10–19, 2014.
- [90] D. S. Novikov and V. G. Kiselev, “Surface-to-volume ratio with oscillating gradients,” *Journal of magnetic resonance*, vol. 210, no. 1, pp. 141–145, 2011.
- [91] M. Schachter, M. Does, A. Anderson, and J. Gore, “Measurements of restricted diffusion using an oscillating gradient spin-echo sequence,” *Journal of magnetic resonance*, vol. 147, no. 2, pp. 232–237, 2000.
- [92] E. X. Wu and M. M. Cheung, “Mr diffusion kurtosis imaging for neural tissue characterization,” *NMR in Biomedicine*, vol. 23, no. 7, pp. 836–848, 2010.
- [93] D. Wu, Q. Li, F. J. Northington, and J. Zhang, “Oscillating gradient diffusion kurtosis imaging of normal and injured mouse brains,” *NMR in Biomedicine*, vol. 31, no. 6, p. e3917, 2018.
- [94] G. K. Yang, T. Ek, F. Eric, F. Thomas, and J. McNab, “Measuring time-dependent diffusion kurtosis using the magnus high-performance head gradient,” in *Proceedings of the 28th Annual Meeting of ISMRM, Virtual*, p. 0962, 2020.
- [95] M. Weiger, J. Overweg, M. B. Rösler, R. Froidevaux, F. Hennel, B. J. Wilm, A. Penn, U. Sturzenegger, W. Schuth, M. Mathlener, *et al.*, “A high-performance gradient insert for rapid and short-t2 imaging at full duty cycle,” *Magnetic resonance in medicine*, vol. 79, no. 6, pp. 3256–3266, 2018.
- [96] J. Veraart, D. S. Novikov, D. Christiaens, B. Ades-Aron, J. Sijbers, and E. Fieremans, “Denoising of diffusion mri using random matrix theory,” *Neuroimage*, vol. 142, pp. 394–406, 2016.
- [97] S. M. Smith, “Fast robust automated brain extraction,” *Human brain mapping*, vol. 17, no. 3, pp. 143–155, 2002.
- [98] B. B. Avants, N. J. Tustison, G. Song, P. A. Cook, A. Klein, and J. C. Gee, “A reproducible evaluation of ants similarity metric performance in brain image registration,” *Neuroimage*, vol. 54, no. 3, pp. 2033–2044, 2011.
- [99] J. M. Bland and D. Altman, “Statistical methods for assessing agreement between two methods of clinical measurement,” *The lancet*, vol. 327, no. 8476, pp. 307–310, 1986.
- [100] M. Nilsson, F. Szczepankiewicz, J. Brabec, M. Taylor, C.-F. Westin, A. Golby, D. van Westen, and P. C. Sundgren, “Tensor-valued diffusion mri in under 3 minutes: an initial survey of microscopic anisotropy and tissue heterogeneity in intracranial tumors,” *Magnetic resonance in medicine*, vol. 83, no. 2, pp. 608–620, 2020.

- [101] S. Y. Huang, Q. Tian, Q. Fan, T. Witzel, B. Wichtmann, J. A. McNab, J. D. Bireley, N. Machado, E. C. Klawiter, C. Mekkaoui, *et al.*, “High-gradient diffusion mri reveals distinct estimates of axon diameter index within different white matter tracts in the in vivo human brain,” *Brain Structure and Function*, vol. 225, no. 4, pp. 1277–1291, 2020.
- [102] D. Graf von Keyserlingk and U. Schramm, “Diameter of axons and thickness of myelin sheaths of the pyramidal tract fibres in the adult human medullary pyramid,” *Anatomischer Anzeiger*, vol. 157, no. 2, pp. 97–111, 1984.
- [103] O. Reynaud, “Time-dependent diffusion mri in cancer: tissue modeling and applications,” *Frontiers in Physics*, vol. 5, p. 58, 2017.
- [104] Y. Lee, B. J. Wilm, D. O. Brunner, S. Gross, T. Schmid, Z. Nagy, and K. P. Pruessmann, “On the signal-to-noise ratio benefit of spiral acquisition in diffusion mri,” *Magnetic Resonance in Medicine*, vol. 85, no. 4, pp. 1924–1937, 2021.
- [105] W. Wu, B. A. Poser, G. Douaud, R. Frost, M.-H. In, O. Speck, P. J. Koopmans, and K. L. Miller, “High-resolution diffusion mri at 7t using a three-dimensional multi-slab acquisition,” *NeuroImage*, vol. 143, pp. 1–14, 2016.

Kevin Borsos

Curriculum Vitae

Education

Master of Science (Medical Biophysics) 2019-2021
Schulich School of Medicine and Dentistry
Western University
London, Ontario

Bachelor's of Science (Biophysics) 2015-2019
Department of Physics and Astronomy
York University
Toronto, Ontario

Awards

- Queen Elizabeth II Graduate Scholarship in Science and Technology 2020-2021
- Imaging Network Ontario Honourable Mention - Oral Presentation 2020
- Western Graduate Research Scholarship (WGRS) 2019, 2020, 2021

Research Contributions

KB Borsos, DHY Tse, PI Dubovan, CA Baron. *A tale of two frequencies: optimizing oscillating gradients for frequency dependent differential kurtosis mapping* [Digital Poster #3640], International Society for Magnetic Resonance in Medicine Annual Meeting & Exhibition, Virtual (May 2021)

N Rahman, K Xu, NJJ Arezza, **KB Borsos**, M Budde, A Brown, CA Baron *Microstructural Diffusion MRI in Mouse Models of Severe and Repetitive Mild Traumatic Brain Injury* [Digital Poster #2040] International Society for Magnetic Resonance in Medicine

Annual Meeting & Exhibition, Virtual (May 2021)

KB Borsos, DHY Tse, PI Dubovan, CA Baron. *Optimized oscillating gradients for frequency dependent in vivo diffusion kurtosis measurement* [Oral Presentation], 19th Annual Symposium Imaging Network Ontario, Virtual (March 2021)

N Rahman, K Xu, NJJ Arezza, **KB Borsos**, A Brown, CA Baron *Microstructural Diffusion MRI in Mouse Models of Severe and Repetitive Mild Traumatic Brain Injury* [Oral Presentation], 19th Annual Symposium Imaging Network Ontario, Virtual (March 2021)

KB Borsos, CA Baron. *Simulation of Spectral Modification for Suppressing CSF in Oscillating Gradient Diffusion MRI* [Oral Presentation], 18th Annual Symposium Imaging Network Ontario, Virtual (March 2020)